JGP Journal of General Physiology

ARTICLE

Asymmetric contribution of a selectivity filter gate in triggering inactivation of $Ca_V1.3$ channels

Pedro J. del Rivero Morfin[1], Audrey L. Kochiss[1], Klaus R. Liedl[2], Bernhard E. Flucher[3], Monica L.I. Fernández-Quintero[2], and Manu Ben-Johny[1]

Voltage-dependent and Ca^{2+}-dependent inactivation (VDI and CDI, respectively) of Ca_V channels are two biologically consequential feedback mechanisms that fine-tune Ca^{2+} entry into neurons and cardiomyocytes. Although known to be initiated by distinct molecular events, how these processes obstruct conduction through the channel pore remains poorly defined. Here, focusing on ultrahighly conserved tryptophan residues in the interdomain interfaces near the selectivity filter of $Ca_V1.3$, we demonstrate a critical role for asymmetric conformational changes in mediating VDI and CDI. Specifically, mutagenesis of the domain III–IV interface, but not others, enhanced VDI. Molecular dynamics simulations demonstrate that mutations in distinct selectivity filter interfaces differentially impact conformational flexibility. Furthermore, mutations in distinct domains preferentially disrupt CDI mediated by the N- versus C-lobes of CaM, thus uncovering a scheme of structural bifurcation of CaM signaling. These findings highlight the fundamental importance of the asymmetric arrangement of the pseudotetrameric Ca_V pore domain for feedback inhibition.

Introduction

The high voltage–activated Ca^{2+} channels ($Ca_V1/2$) serve as vital conduits for Ca^{2+} entry responsible for orchestrating diverse physiological processes, ranging from excitation–contraction coupling in muscle (Bers, 2002) to vesicle secretion and gene transcription in neurons (Berridge et al., 2000; Dolmetsch, 2003). Molecularly, the eukaryotic $Ca_V1/2$ channels possess a conspicuous pseudotetrameric architecture that is thought to permit asymmetric conformational changes to fine-tune channel activity (Catterall et al., 2017). For related voltage-gated Na^+ (Na_V) channels, this asymmetric architecture allows distinct voltage-sensing domains (VSDs) to differentially impact activation versus inactivation and pore conformation (Goldschen-Ohm et al., 2013). By comparison, although Ca_V channels have VSDs with distinct kinetics, the importance of the overall pseudotetrameric architecture and potential asymmetric conformational changes are not fully established, though likely important (Tuluc et al., 2016; Fernández-Quintero et al., 2021; Savalli et al., 2021). Like Na_V, Ca_V channels are subject to exquisite feedback regulatory mechanisms, including both voltage-dependent inactivation (VDI) and Ca^{2+}-dependent inactivation (CDI) that limits excessive Ca^{2+} entry into the cell (Minor and Findeisen, 2010; Ben-Johny and Yue, 2014). Both processes are biologically consequential as Ca^{2+} channelopathies involve deficits in inactivation that disrupt electrical signaling and Ca^{2+} homeostasis, thereby contributing to neurological, neurodevelopmental, and cardiac arrhythmogenic disorders such as Timothy syndrome (TS; Barrett and Tsien, 2008; Dick et al., 2012; Limpitikul et al., 2014; Pinggera et al., 2015). Both inhibitory processes have disparate molecular origins. VDI is initiated by voltage-dependent conformational changes triggered by the movement of the four homologous transmembrane voltage-sensing domains (Stotz and Zamponi, 2001; Stotz et al., 2004; Tadross et al., 2010). By contrast, CDI is largely independent of voltage (Tadross and Yue, 2010) and, instead, ensues from Ca^{2+} binding to the two lobes of calmodulin (CaM) tethered to the Ca_V C-terminus (Peterson et al., 1999; Qin et al., 1999; Zühlke et al., 1999). These processes converge on distinct "gates" in the pseudosymmetric pore domain to obstruct ion influx (Tadross et al., 2010; Abderemane-Ali et al., 2019). Even so, the exact nature of conformational changes that underlie channel feedback inhibition and the contribution of the pseudosymmetric channel architecture are not fully understood.

[1]Department of Physiology and Cellular Biophysics, Columbia University, New York, NY, USA; [2]Institute of General, Inorganic and Theoretical Chemistry, University of Innsbruck, Innsbruck, Austria; [3]Department of Physiology and Medical Physics, Institute of Physiology, Medical University Innsbruck, Innsbruck, Austria.

Correspondence to Manu Ben-Johny: mbj2124@cumc.columbia.edu; Monica L.I. Fernández-Quintero: monica.fernandez-quintero@uibk.ac.at

This work is part of a special issue on Structure and Function of Ion Channels in Native Cells and Macromolecular Complexes.

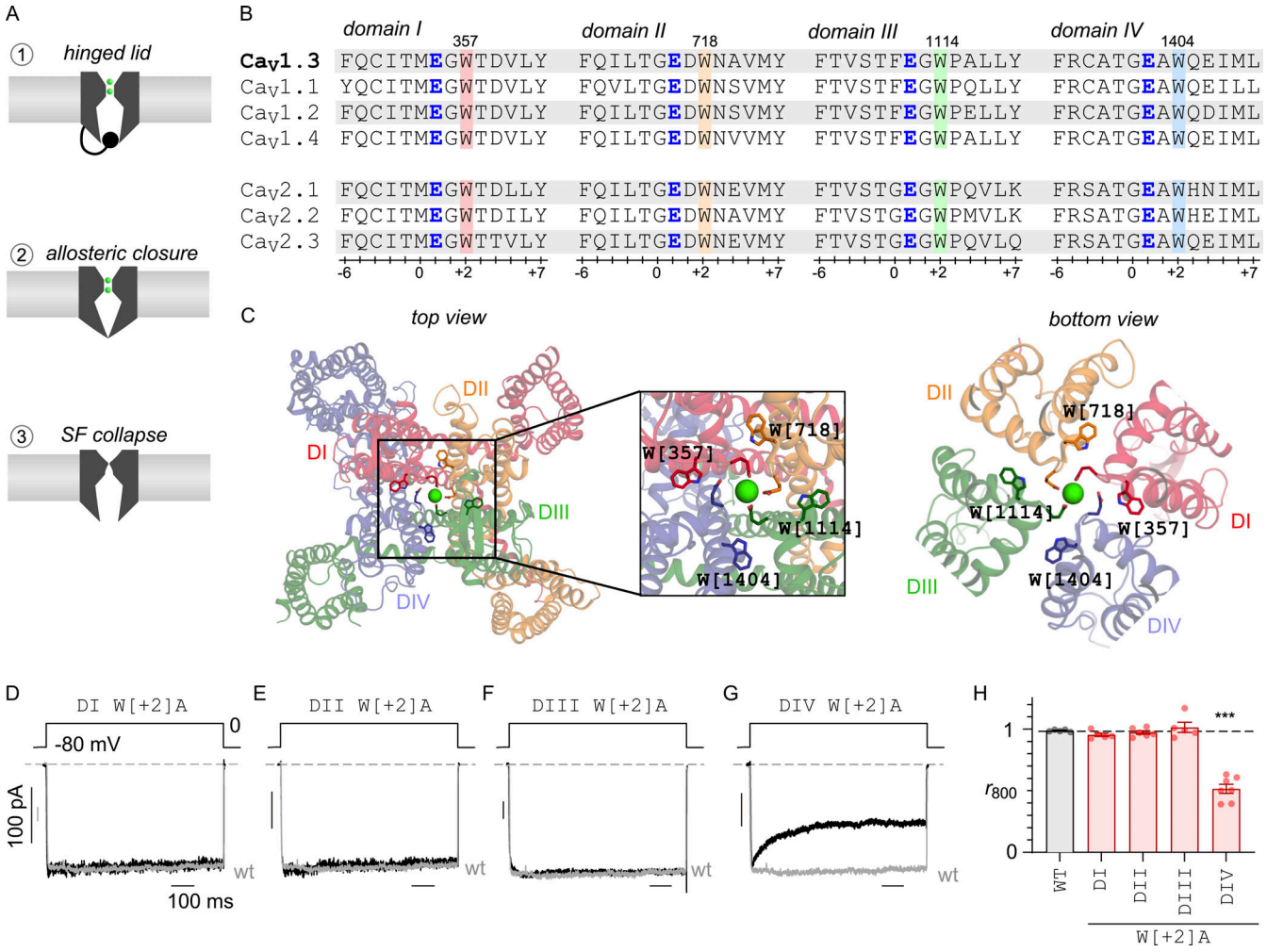

Figure 1. **Asymmetric role of DIV pore helix in tuning VDI of $Ca_V1.3$. (A)** Three distinct end-stage mechanisms for $Ca_V1.3$ inactivation. Scheme 1 shows a hinged-lid mechanism where the pore is occluded by an inactivation particle (DI–DII linker), scheme 2 shows an allosteric mechanism where the open probability is reduced through increased channel closure, and scheme 3 shows selectivity filter collapse. **(B)** Sequence alignment shows the conservation of a tryptophan residue (W) in the pore segment adjacent to the putative Ca^{2+} coordinating glutamate (E) residue. **(C)** Structural models show the pseudo-tetrameric architecture of $Ca_V1.3$ (PDB ID 7UHG). The inset shows the ion conduction pathway lined by the selectivity filter Ca^{2+} coordinating glutamate residues and the spatial location of the conserved tryptophan. **(D)** Representative Ba^{2+} current traces evoked in response to an 800-ms voltage step to 0 mV show minimal VDI of both wild-type (gray) and DI W[+2]A mutant channels. The wild-type current is normalized to compare inactivation kinetics. **(E and F)** Similarly, both DII W[+2]A and DIII W[+2]A mutant channels also showed minimal VDI. Format as in panel C. **(G)** By contrast, DIV W[+2]A mutation enhanced VDI of $Ca_V1.3$. Format as in panel C. **(H)** Population data shows the fraction of remaining current following 800-ms depolarization (r_{800}). The DIV W[+2]A mutation selectively increases inactivation in comparison to both wild-type (gray) and W[+2]A substitutions in DI–DIII. Each bar, mean ± SEM. Wild-type, n = 5 cells, DI W[+2]A, n = 5 cells, DII W[+2]A, n = 6 cells, DIII W[+2]A, n = 5 cells, DIV W[+2]A, n = 7 cells. ***P < 0.001 by Tukey's multiple comparisons test.

Three end-stage mechanisms of inactivation have been proposed, paralleling findings with related ion channels (Fig. 1 A). These include (1) a hinged-lid mechanism that involves a cytosolic inactivation particle that occludes the ion conduction pathway (Stotz et al., 2000) similar to N-type inactivation of Shaker K^+ channels (Hoshi et al., 1990) or fast inactivation of Na_V channels (West et al., 1992; Yan et al., 2017), (2) an allosteric closure or destabilization of the S6 activation gate (Imredy and Yue, 1994; Tadross et al., 2010) similar to allosteric regulation of K_V7 channels (Zaydman and Cui, 2014), and (3) a conformational rearrangement of the selectivity filter (SF; Abderemane-Ali et al., 2019), akin to P-type (or C-type) inactivation in Shaker K^+ channels (Hoshi et al., 1991) or slow inactivation of Na_V channels (Balser et al., 1996). For VDI, a hinged-lid mechanism has been proposed (scheme 1), with the N-terminus of the intracellular domain I–II (DI–DII) linker serving as an inactivation particle that binds to a transmembrane receptor site formed by the S6 gate (Stotz et al., 2000; Dafi et al., 2004; Tadross et al., 2010). For CDI, initial studies indicated an allosteric mechanism, where channels switch to a distinct gating pattern with sparse openings (scheme 2; Imredy and Yue, 1994; Tadross et al., 2010). More recently, structure-guided mutagenesis experiments point to the involvement of an alternate SF gate for both VDI and CDI (scheme 3; Abderemane-Ali et al., 2019). Even so, the extent of SF conformational changes in channel feedback inhibition and key factors that govern this process remains to be fully understood.

Here, we sought to delineate the functional importance of conformational changes in the SF in mediating both VDI and

CDI. We focused on $Ca_V1.3$ channels for two reasons. First, these channels exhibit characteristically slow VDI kinetics owing to the presence of a "shield" that counteracts a hinged-lid inactivation mechanism (Tadross et al., 2010). This permits a bottom-up approach, whereby VDI may be engineered, thereby allowing us to probe the functional role of the SF gate. Second, these channels also demonstrate robust CDI that depends on distinct conformational changes involving both the N- and C-lobes of CaM. We considered an ultrahighly conserved Trp residue (W[+2]) within the SF found at the interface between the pore helices from different domains (Payandeh and Minor, 2015; Fig. 1, B and C). Systematic mutagenesis of the corresponding residue in each domain revealed an asymmetric switch in the pore domain that upregulates VDI. Furthermore, in depth analysis of CDI showed that mutating the W[+2] residue in distinct domains asymmetrically diminished CDI mediated by distinct CaM lobes. Of pathophysiological relevance, we further show that destabilizing the SF gate could reverse deficits in inactivation linked to TS. In all, these findings highlight the fundamental importance of the asymmetric arrangement of the pseudotetrameric $Ca_V1.3$ pore domain for channel inactivation.

Materials and methods

Molecular biology

Mutagenesis $Ca_V1.3$ was performed using the truncated variant of rat $Ca_V1.3$ (AF370009.1), $Ca_V1.3_{\Delta1626}$, as previous published (Tadross et al., 2010; Ben-Johny et al., 2013). Briefly, we first PCR-amplified subsegments of wild-type $Ca_V1.3$ containing SF domains of DI and DII (R1, flanked by restriction enzyme sites BsiWI and Eco47III), DIII (R2, flanked by restriction enzyme sites Eco47III and BglII), and DIV (R3, flanked by restriction enzyme sites BglII and XbaI), respectively. These subsegments were inserted into the pCRBlunt II-TOPO vector using the Zero Blunt TOPO PCR cloning kit (Invitrogen). Point mutations in respective $Ca_V1.3$ subsegments were then generated using Quikchange II kit (Agilent). We generated W357A and W718A and used R1 plasmid, while R2 plasmid was used for W1114A and R3 plasmid for W1404A, W1404F, W1404V, and W1404T mutations. Subsequently, the mutated segments were ligated into the wild-type $Ca_V1.3$ following restriction digest with the specific enzymes for a given subsegment. Ligates were then transformed into either XL10-Gold Ultracompetent Cells (Agilent) or DH5α Competent Cells (Thermo Fisher Scientific), plated, and cultured in selective LB broth. DNA was extracted and purified from cultures using either QIAprep Spin Miniprep Kit (Qiagen) or GeneJET PCR Purification Kit (Thermo Fisher Scientific). Sanger sequencing was used to verify each mutant. For T1107Q/W1404A double mutant, we first generated the T1107Q mutation using Quikchange II (Agilent) in the R2 subsegment. Subsequently, this region was ligated into the W1404A mutant channel following restriction digest using Eco47III and BglII. Human $Ca_V1.2$ and the G406R mutant were generously gifted by Dr. Ivy Dick as were previously published (Dick et al., 2016). DIV W[+2]A mutation corresponding to residue 1,466 was generated on the G406R mutant background using Quickchange II (Agilent).

Cell culture and transfection

For whole-cell electrophysiology, HEK293 cells were cultured on glass coverslips in 60-mm dishes and transfected using a calcium phosphate method. We applied 2–8 µg of cDNA encoding the desired channel α_1 subunit (WT or engineered variant), along with 4 µg of rat β subunit (β_{1b}, β_{2a}, β_3, or β_4) and 4 µg of rat brain $\alpha_2\delta_1$ (NCBI accession no. NM012919.2). In experiments that required CaM expression, we transfected 2–4 µg of cDNA encoding CaM WT or mutant variants (CaM_{12}, CaM_{34}, or CaM_{1234}). To enhance the expression, cDNA for simian virus 40 T antigen (0.5 µg) was cotransfected. Electrophysiology recordings were done at room temperature 1–3 d after transfection.

Whole-cell recordings

Whole-cell voltage-clamp recordings for HEK293 were collected at room temperature using an Axopatch 200B amplifier (Axon Instruments). Glass pipettes (MTW 150-F4, World Precision Instruments) were pulled with a horizontal puller (P97; Sutter Instruments Co.) and fire-polished (Microforge; Narishige), resulting in 1–3-MΩ resistances, before series resistance compensation of 70%. Internal solutions contained 135 mM $CsMeSO_3$, 5 mM $CsCl_2$, 1 mM $MgCl_2$, 4 mM MgATP, 10 mM HEPES, and 10 mM BAPTA, adjusted to 290–295 mOsm with $CsMeSO_3$ and pH 7.4 with CsOH. The external solutions contained 140 mM TEA-$MeSO_3$, 10 mM HEPES (pH 7.4), and either 40 mM $CaCl_2$ or $BaCl_2$. This external solution composition was chosen based on previous studies to ensure that local Ca^{2+} signals are saturated to drive maximal local CDI (Tadross et al., 2008). For experiments using Na^+ as a charge carrier, we used an external solution containing 140 mM NaCl, 10 mM HEPES (pH 7.4), 10 mM TEA-$MeSO_3$, and 0.5 mM EGTA. Solutions were adjusted to 300 mosM with TEA-$MeSO_3$ and pH 7.4 with TEA-OH. For CDI and VDI measurements, we used a family of test pulses from −50 to +50 mV with repetition intervals of 20–120 s from a holding potential of −80 mV. Custom MATLAB (Mathworks) software was used to determine peak current and fraction of peak current remaining after either 300 ms (r_{300}) of depolarization or 800 ms (r_{800}) of depolarization. Residual currents after depolarization were measured at +10 mV after an initial pulse of +10 mV for 15 ms followed by a family of test pulses from −60 to +50 mV for 800 ms. Custom MATLAB (Mathworks) software was used to determine peak current and I_2/I_1 ratio. As W[1404]A mutation itself enhanced VDI, quantifying CDI (i.e., the CaM-driven component of inactivation) by comparing inactivation with Ba^{2+} versus Ca^{2+} as the charge carrier is imprecise. Accordingly, we estimated baseline VDI for W[1404]A mutation in the presence of Ca^{2+} by coexpressing CaM_{1234} ($r_{300,CaM1234} = I_{300ms}/I_{peak}$ and $r_{800,CaM1234} = I_{800ms}/I_{peak}$), where I_{peak} is the peak current, and I_{300} and I_{800} are current levels following 300 ms or 800 ms of depolarization, respectively. We then measured total inactivation (CDI and VDI) with Ca^{2+} as the charge carrier with endogenous CaM, CaM_{12}, or CaM_{34} to isolate total, C- and N-lobe components of CDI, respectively ($r_{300,Ca} = I_{300ms}/I_{peak}$ and $r_{800,Ca} = I_{800ms}/I_{peak}$, with Ca^{2+} as the charge carrier). Subsequently, CDI was estimated as ($CDI_{300} = 1 - r_{300,Ca}/r_{300,CaM1234}$) or ($CDI_{800} = 1 - r_{800,Ca}/r_{800,CaM1234}$). For all other mutations, we observed minimal VDI. As such CDI was measured as CDI_{300} =

$1 - r_{300,Ca}/r_{300,Ba}$ and $CDI_{800} = 1 - r_{800,Ca}/r_{800,Ba}$. For these experiments, the experimenter was not blinded to the specific experimental condition as transfected cells included a fluorescent reporter. Data from different conditions were acquired in a random order. For each condition, we obtained data from at least two independent transfections.

Molecular dynamics simulations

As starting structures for our simulations, we used the recently published cryo-EM structure of the $Ca_V1.3$ Ca^{2+} channel complex (PDB accession code: 7UHG; Yao et al., 2022). The structures of the W1404A and the W718A mutants were derived from the wild-type model by replacing the mutated residue followed by a local energy minimization using MOE (Molecular Operating Environment, version 2020.09; Molecular Computing Group, Inc.). The C- and N-terminal parts of each domain were capped with acetylamide (ACE) and N-methylamide to avoid perturbations by free-charged functional groups. The structure model was embedded in a plasma membrane consisting of POPC (1-palmitoyl-2-oleoyl-sn-glycero-3-phosphocholine) and cholesterol in a 3:1 ratio using the CHARMM-GUI Membrane Builder (Jo et al., 2008, 2009). Water molecules and 0.15 M $CaCl_2$ were included in the simulation box. Energy minimizations of wild-type and mutant structures in the membrane environment were performed. The topology was generated with the LEaP tool of the AmberTools21 using force fields for proteins and lipids, ff14SBonlysc and Lipid14, respectively (Dickson et al., 2014). The wild-type and mutant structures were gradually heated from 0 to 300 K in two steps, keeping the lipids fixed, and then equilibrated over 1 ns. Then molecular dynamics simulations were performed for 3 × 300 ns, with time steps of 2 fs at 300 K and in anisotropic pressure scaling conditions. Van der Waals and short-range electrostatic interactions were cut off at 10 Å, whereas long-range electrostatics were calculated by the Particle Mesh Ewald (PME) method. PyMOL was used to visualize the key interactions and point out differences in the wild-type and mutant structures (The PyMOL Molecular Graphics System; Version 2.0 Schrödinger, LLC).

Online supplemental material

Fig. S1 shows that mutations in $Ca_V1.3$ DI–DIV SF mutations minimally alter channel activation. Fig. S2 shows an extended biophysical characterization of $Ca_V1.3$ DIV W[+2]A mutant, including an in-depth assessment of inactivation using Ca^{2+} and Na^+ as charge carriers.

Results

Mutations in the pore domain tune inactivation of $Ca_V1.3$

Previous studies have identified the presence of a highly conserved Trp (W[+2]) residue, two residues downstream of the selectivity filter of Ca_V, Na_V, and NALCN channels (Payandeh and Minor, 2015). Fig. 1 B shows sequence alignment confirming the preservation of this residue within all four domains of Ca_V channels, while Fig. 1 C shows its structural location within the interdomain interfaces. We individually substituted W[+2] residues in DI–DIV of $Ca_V1.3$ with alanine, yielding W[357]A, W[718]A, W[1114]A, and W[1404]A mutant channels, respectively. For convenience, we refer to these mutations by the nomenclature: D*x* W[*y*]A where *x* denotes the particular domain and *y* refers to the position relative to the central Glu that forms the SF. To probe changes in VDI, we transfected either wild-type or mutant channels in HEK293 cells and undertook whole-cell current recordings utilizing Ba^{2+} as the charge carrier. Here, we cotransfected both $\alpha_2\delta_1$ and β_{2A} subunits as they are essential for trafficking and proper function of the $Ca_V1.3$ channel. Importantly, the β subunit is well known to tune inactivation properties. As such for these experiments, we chose β_{2A}, a palmitoylated variant that strongly reduces inactivation compared with other β subunit isoforms (Olcese et al., 1994; Chien et al., 1996; Colecraft et al., 2002; Van Petegem et al., 2004; He et al., 2007). As Ba^{2+} binds poorly to calmodulin (Chao et al., 1984), the use of this charge carrier permits quantification of VDI independent of CDI. For the wild-type $Ca_V1.3$ short variant, an 800-ms voltage step to 0 mV revealed rapid activation and minimal inactivation, consistent with previous studies (Fig. 1 D, gray trace). Similarly, analysis of DI W[+2]A, DII W[+2]A, and DIII W[+2]A mutant channels also revealed minimal VDI (Fig. 1, D–F, black traces). By contrast, exemplar current recordings with the DIV W[+2]A mutant showed a rapid decay of Ba^{2+} currents following initial activation, demonstrating increased inactivation (Fig. 1 G, black trace). To quantify the steady-state extent of inactivation, we computed the ratio of the current remaining following 800 ms of depolarization with that of the peak value (r_{800}). Population data confirmed a significant increase in inactivation with the DIV W[+2]A mutation, manifesting as a reduced r_{800} value, in comparison with wild-type and other mutant channels (Fig. 1 H). For all mutants, we observed minimal changes in the normalized current–voltage relationship suggesting a minimal effect of the SF mutations on channel activation (Fig. S1). These findings suggest that the pore domain constitutes a key structural determinant for VDI in $Ca_V1.3$. Furthermore, the selective effect of DIV W[+2]A in enhancing VDI highlights the functional asymmetry of pore domain conformational changes.

Distinct functional signature of SF-dependent VDI of $Ca_V1.3$

Canonical VDI of $Ca_V1/2$ channels follow a Boltzmann relationship with voltage, whereby currents evoked at more depolarizing potentials exhibit stronger inactivation (Imredy and Yue, 1994). We, therefore, sought to determine whether enhanced $Ca_V1.3$ VDI resulting from the pore-domain mutation also follows a similar trend. As such, the inactivation of $Ca_V1.3$ DIV W[+2]A mutant channels was determined by measuring fractional decay of whole-cell Ba^{2+} currents evoked in response to a family of step-depolarizations (Fig. 2, A and B). Normalizing each current trace to its peak value showed that the extent of inactivation was reduced for DIV W[+2]A mutant at higher potentials but not wild-type channels (Fig. 2, A and B; and Fig. S2 A). To further quantify the voltage dependence of inactivation, we utilized a two-pulse protocol (Fig. 2, C–F; Patil et al., 1998). A brief 15-ms prepulse to 10 mV is used to probe the available current prior to VDI (I_{pre}; Fig. 2 C and Fig. S2 B). A family of 800-ms step depolarizations to various test-pulse potentials (V_{test}) is

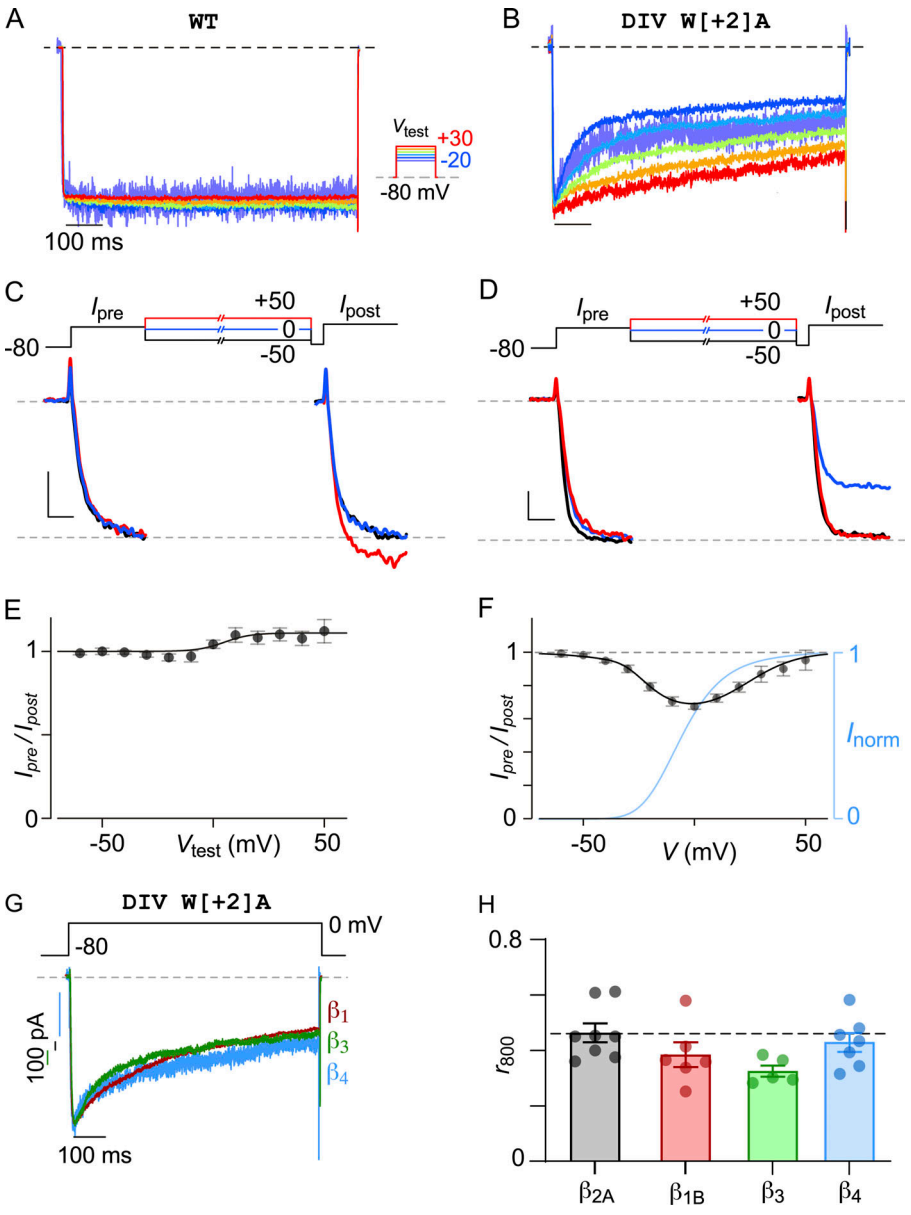

Figure 2. **Distinct functional signature of $Ca_V1.3$ VDI. (A and B)** Exemplar Ba^{2+} current traces evoked in response to a family of voltage-steps show VDI of both wild-type $Ca_V1.3$ (panel A) and DIV W[+2]A mutant (panel B). CaM_{1234} coexpressed to exclude the potential contribution of CDI. **(C)** A two-pulse protocol is used to quantify the voltage dependence of inactivation. Comparison of Ba^{2+} currents for wild-type $Ca_V1.3$ during the prepulse versus the postpulse. $Ca_V1.3$ currents are increased in response to higher test-pulse potentials. See Fig. S2 B for full exemplar trace. **(D)** DIV W[+2]A mutant channels exhibit diminished peak currents during the postpulse following test pulse to intermediate voltages. See Fig. S2 C for a full exemplar trace. **(E)** Analysis of wild-type $Ca_V1.3$ reveals minimal VDI across multiple voltages. For each dot and error, mean ± SEM n = 7. **(F)** VDI of DIV W[+2]A mutation exhibits a U-shaped voltage-dependence with the strongest inactivation observed near 0 mV. Blue curve, voltage-dependence of inactivation obtained from the whole cell normalized IV relations (Fig. S2 E). For each dot and error, mean ± SEM n = 7 cells. **(G)** Exemplar traces show similar kinetics of inactivation for DIV W[+2]A mutant in the presence of various β subunits. **(H)** Population data confirms minor differences in VDI quantified as r_{800} measured at 0 mV in the presence of various β subunits. Each bar and error, mean ± SEM. n = 6 cells (β_{1B}), n = 8 cells (β_{2A}), n = 5 cells (β_3), n = 7 cells (β_4). P = 0.076 by one-way ANOVA.

then used to elicit steady-state levels of inactivation, while a 15-ms postpulse to 10 mV measures the residual current, reflecting ion influx through non-inactivated channels. The strength of VDI is quantified as the ratio of peak current during the postpulse (I_{post}) to that during the prepulse (I_{pre}; Fig. S2 B). For wild-type $Ca_V1.3$, we observed a modest increase in peak currents during the postpulse as compared with the prepulse at more depolarized test-potential, indicating the presence of weak voltage-dependent facilitation (Fig. 2, C and E; and Fig. S2 B). By comparison, for the DIV W[+2]A mutant, we observed a U-shaped voltage-dependence of VDI with the largest reduction in peak current observed with modest depolarizations (Fig. 2, D and F; and Fig. S2 C). We further assessed voltage dependence of inactivation with either Ca^{2+} or Na^+ as the charge carrier. In both cases, we observed a U-shaped voltage dependence (Ca^{2+}, Fig. S2, D–F; Na^+, Fig. S2, G–I). Of note, for these experiments, we coexpressed Ca^{2+}-insensitive mutant CaM (CaM_{1234}) whose Ca^{2+} binding sites in its EF hands were disabled (Xia et al., 1998; Peterson et al., 1999). As this maneuver disables CDI, it allows us to dissect the CaM-independent effects of Ca^{2+} on channel gating.

Conventional VDI of $Ca_V1/2$ channels is highly tuned by the auxiliary β-subunit associated with the channel. More specifically, membrane-localized β-subunits (e.g., palmitoylated β_{2A}) reduce VDI, while other isoforms yield strong VDI. For $Ca_V1.3$, we previously identified mutations in the distal S6 gate that enhanced VDI (Tadross et al., 2010). However, the magnitude of VDI for these mutations varied depending on the specific β-subunit coexpressed. Here, to determine whether VDI conferred by SF mutation is also tuned by the auxiliary β-subunit, we coexpressed $Ca_V1.3$ DIV W[+2]A mutant with non-membrane localized β_1, β_3, or β_4 subunits. In all cases, we found that the extent of VDI was not further accentuated compared to that with the β_{2A} subunit (Fig. 2, G and H). Taken together, these findings

suggest that VDI conferred by SF mutation is a biophysically distinct process compared with conventional VDI of Ca_V1 and Ca_V2 channels.

DIV W[+2]A mutation increases conformational flexibility of the SF

Given the asymmetric effect of DIV W[+2] residue and its location at the interface of two domains, we considered whether this mutation destabilizes the conformation of the SF. To probe this possibility, we performed molecular dynamics (MD) simulations (3 × 300 ns) based on the recently published cryo-EM structure of the $Ca_V1.3$ channel (Yao et al., 2022). We considered both WT and the mutant channels embedded in a lipid bilayer. This cryo-EM structure has a global resolution of ∼3 Å and the local quality of the electron density maps suggests that this region is well resolved. To quantify potential changes in flexibility upon substitution of tryptophan residues with alanine, we used the obtained simulations to calculate residue-wise B-factors. B-factors are an alignment-dependent measure to identify areas with higher fluctuations or flexibility. In wild-type channels, the two helices of the pore loop are all very rigid (low B-factors; Fig. 3, A, C, E, and G, green), except in DIV, where the P1 helix displays elevated flexibility (higher B-factor; Fig. 3 A, red). In comparison with wild-type channels, the introduction of the DIV W[+2]A mutation increased the local conformational flexibility of this region evident as increased B-factor mapped on the structural model, particularly in the P2 helix (Fig. 3, A and B). This suggests that this mutation destabilizes the SF conformation to potentially initiate inactivation. To evaluate this possibility further, we considered whether similar mutations in the other domains also yielded increased conformational flexibility. In contrast to the DIV W[+2]A, we found that W[+2]A mutations in all other repeats did not appreciably increase the structural variability of the SF and only minimally altered the B-factors (Fig. 3, C–H), suggesting that the conformational stability of the SF is largely preserved by these mutations. Apparently, the increased conformational flexibility of the SF of DIV is not the direct consequence of the amino acid substitution in the P2 helix, rather it depends on the specific environment of the SF in this domain. Interestingly, further scrutiny of the DIV W[+2]A mutant revealed key alterations in the conformation of the Ca^{2+} coordinating E[0] residues that line the SF (Fig. 3 I). Specifically, the DIV E[0] residue shifts away from the center of the ion permeation pathway by ∼4 Å, forming a contact with DI W[+2] residue (W357). This change may disrupt the high-affinity coordination of a Ca^{2+} ion in the SF, ultimately impacting ion influx through the channel. Taken together, these results highlight the asymmetric effect of SF mutations on conformational stability and the unique role of DIV W[+2] mutation for VDI of $Ca_V1.3$.

The bulkiness of the selectivity filter DIV W[+2] residue tunes inactivation

Having inferred that the DIV W[+2]A mutant undergoes a distinct form of inactivation, we sought to dissect its underlying mechanisms. Structurally, the W[1404] residue is wedged at the interface between selectivity filter helices from DIV and DIII (Fig. 1 C). The alanine mutation would remove this wedge and potentially promote conformational changes in the selectivity filter that manifests as channel inactivation. As such, we reasoned that the bulkiness of the W[1404] side chain may be essential to stabilize the selectivity filter and tune inactivation kinetics. We thus replaced the tryptophan residue with a threonine (DIV W[+2]T) and undertook whole-cell recordings. We found that DIV W[+2]T also increased VDI; however, the net magnitude of increase was blunted in comparison to the DIV W[+2]A (Fig. 4 A), consistent with the intermediate size of the threonine side-chain. In like manner, substitution of the DIV W[+2] residue with a valine (DIV W[+2]V) also yielded an intermediate increase in VDI (Fig. 4 B). By contrast, replacing the DIV W[+2] residue with a bulky phenylalanine residue (DIV W[+2]F) yielded no appreciable increase in VDI as compared with wild-type channels (Fig. 4 C). These findings qualitatively confirm the trend that increased bulkiness of the DIV W[+2] residue reduces the magnitude of VDI. To quantify this trend, we plotted the r_{800} values for various DIV W[+2] substitutions as a function of the side-chain accessible surface area (ASA). We found that the r_{800} values increased with increasing ASA and with the substitution of bulkier residues resulting in diminished VDI (Fig. 4 G). This relationship was empirically fit using a Boltzmann function. These findings are consistent with the DIV W[+2] residue serving to stabilize the DIII–DIV SF interface.

To further test this possibility, we hypothesized that introducing bulky side chains to residues in the DIII interface could compensate for the decreased stability resulting from DIV W[+2] A mutation. Accordingly, we identified candidate residues in DIII selectivity filter helices that are within 5 Å of the DIV W[+2] residue. These included residues F[1106] (DIII F[−6]), T[1107] (DIII T[−5]), T[1110] (DIII T[−2]), and E[1112] (DIII E[0]; Fig. 4 E). Examination of corresponding residues in domain I, II, and IV showed that F[−6], T[−2], E[0] are conserved. By contrast, the analogous position of DIII T[−5] residue in domains I, II, and IV is occupied by either a glutamine or an arginine (Fig. 4 E). As such, we replaced T[1107] with a glutamine (T[1107]Q) in DIV W[+2]A mutant channel and probed changes in VDI. Indeed, we found that the DIV W[+2]A/DIII T[−5]Q double mutant exhibited substantially diminished inactivation as compared to DIV W[+2]A mutant channels (Fig. 4, F and G). Taken together, these results suggest that the symmetric W[+2] residues determine the stability of the selectivity filter in concert with the asymmetric inter-domain interface residues. The two together are critical to prevent the collapse of the ion conduction pathway, and thus confer a unique role for DIV in suppressing VDI in $Ca_V1.3$ channels.

Pore domain mutations disrupt CDI in a calmodulin lobe-specific manner

Distinct from VDI, $Ca_V1.3$ channels undergo rapid CDI mediated by CaM. Recent studies suggest that the end-stage mechanism of CDI relies on conformational changes in the selectivity filter (Abderemane-Ali et al., 2019). Given the proximity of the tryptophan residues in the structure of the selectivity filter to the Ca^{2+} coordinating residues, we considered whether these mutations also alter CDI. At baseline, $Ca_V1.3$ channels exhibit strong CDI (Fig. 5 A, rose curve) quantified as the fraction of excess inactivation with Ca^{2+} versus Ba^{2+} as charge carrier measured

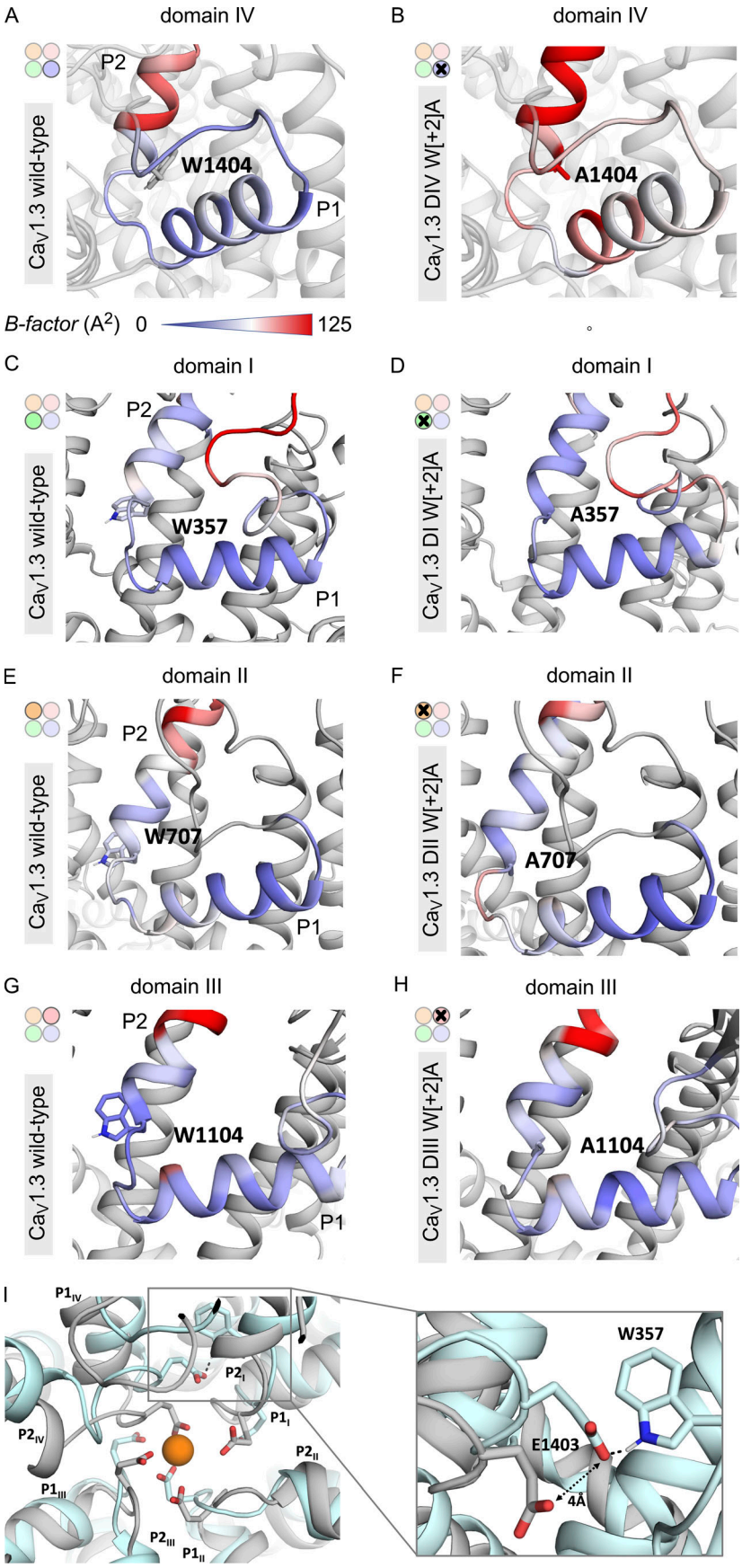

Figure 3. **DIV W[+2]A mutation increases local conformational flexibility near the selectivity filter. (A)** MD simulations were used to estimate the local conformational flexibility of the DIV pore helices of wild-type $Ca_V1.3$ embedded in a lipid bilayer. Colormap indicates computed B-factors for residues in DIV pore helices ranging from 0 (green) to 147.7 (red) corresponding to increasing flexibility. **(B)** DIV W[+2]A mutation increases local conformational flexibility. **(C and D)** In comparison to wild-type channels (panel C), simulations of DI W[+2]A mutant (panel D) show minimal change in computed B-factors for residues in DII pore helices. **(E and F)** Both wild-type (panel E) and DII W[+2]A mutant (panel F) show minimal change in local conformational flexibility. **(G and H)** Similarly, both wild-type (panel G) and DII W[+2]A mutant (panel H) exhibit minimal change in local conformational flexibility. This differential effect between DI–III versus DIV points to a specific role for DIV in tuning VDI. **(I)** Left: Comparison of wild-type versus DIV W[+2]A mutation reveals key changes in the selectivity filter conformation. The DIV W[+2]A mutation alters the arrangement of Ca^{2+} coordinating E[0] residue, with DIV E[0] residue shifted by ~4 Å. Right: Detailed view of the DIV E[0] residue (E1402).

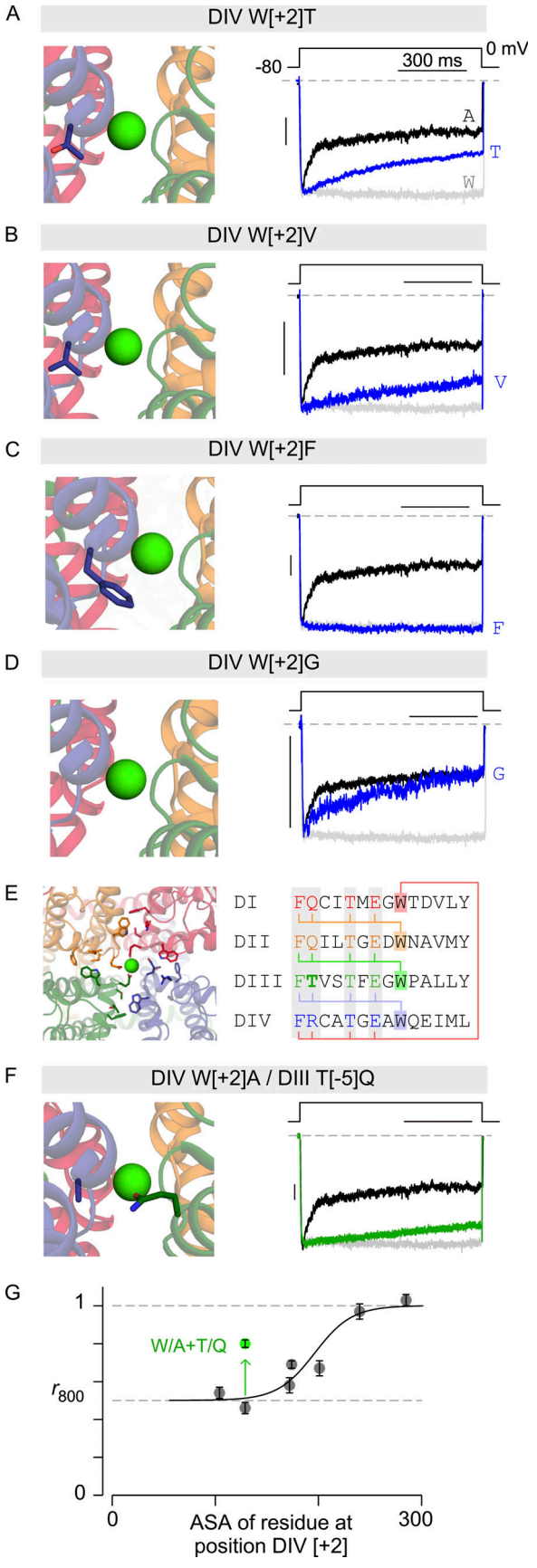

Figure 4. **Bulkiness of the DIV W[+2] residue tunes VDI. (A)** Exemplar traces reveal intermediate inactivation of $Ca_V1.3$ DIV W[+2]T mutant (blue). Exemplar traces from wild-type (W[+2]) and DIV W[+2]A mutant channels are reproduced from Fig. 1 F to facilitate comparison. **(B)** VDI is similarly diminished for DIV W[+2]V mutation. Format as in panel A. **(C)** VDI is virtually absent for DIV W[+2]F mutation. **(D)** VDI is enhanced for DIV W[+2]G mutation. **(E)** Left: Structural model highlights residues in adjacent domains that are within 5 Å of W[+2] residue in a given domain. Right: Sequence alignment and residues in close vicinity of W[+2] residue. Neighborhood residues E[0], T[−2], and F[−6] are conserved across different domains. By contrast, DIV W[+2] is in the vicinity of DIII T[−5] while either a Q or an R is present at the −5 position of other domains. **(F)** Analysis of DIII T[−5]Q/DIV W[+2]A double mutation shows reduced VDI in comparison with DIV W[+2]A single mutation. **(G)** Population r_{800} values for DIV W[+2] mutations reveal a Boltzmann relation between VDI as the accessible side-chain surface area. DIII T[−5]Q/DIV W[+2]A reduced VDI in comparison to DIV W[+2]A mutation and deviates from this relationship. Each symbol and error, mean ± SEM from n = 5 cells for each mutant.

following 300 ms of depolarization ($CDI = 1 - r_{300,Ca}/r_{300,Ba}$). Here, CDI measurements were performed at ambient CaM levels. Analysis of DI W[+2]A, DII W[+2]A, and DIII W[+2]A mutants revealed minimal changes in CDI (Fig. 5, A–C). As DIV W[+2]A mutation enhances VDI, comparison of inactivation kinetics with Ca^{2+} versus Ba^{2+} as permeant ion is insufficient to quantify CDI. To obviate this limitation, we estimated CDI as excess inactivation of Ca^{2+} currents with endogenous CaM compared to with Ca^{2+}-binding deficient CaM_{1234} (see Materials and methods). The latter maneuver disables CDI and provides an estimate of average VDI with Ca^{2+} as permeant ion (Fig. 5 D, blue). Thus measured, the DIV W[+2]A mutant showed a modest but statistically significant reduction in CDI ($P < 0.001$, Fig. 5 E).

As $Ca_V1.3$ CDI is mediated by both N- and C-lobes of CaM (Yang et al., 2006), we next considered whether pore domain mutations may differentially impact regulation by the distinct CaM lobes. To evaluate this possibility, we measured C-lobe CDI by co-expressing mutant CaM_{12} with Ca^{2+} binding to its N-lobe disabled, or N-lobe CDI in the presence of CaM_{34} whose Ca^{2+} binding to the C-lobe is disabled. Indeed, we found that DI W[+2]A, DII W[+2]A, and DIII W[+2]A mutants had minimal or no effect on C-lobe CDI (Fig. 5, F–H and J). However the DIV W[+2]A mutation strongly inhibited C-lobe CDI (Fig. 5, I and J). By contrast, we observed that N-lobe CDI was sharply diminished for DI W[+2]A, DII W[+2]A, and DIII W[+2]A mutants (Fig. 5, K–M and O), while the DIV W[+2]A mutant exhibited an increase in CDI (Fig. 5, N and O). These findings highlight the asymmetric contribution of pore domain residues in differentially coupling CDI triggered by distinct CaM lobes.

DIV W[+2] mutation enhances inactivation of TS-linked $Ca_V1.2$ variant

Human mutations in $Ca_V1.2$ cause a severe multisystem disorder known as TS, marked by an increased likelihood of cardiac arrhythmia and neurological and neurodevelopmental deficits (Splawski et al., 2004). Mechanistically, these channelopathic variants are well established to exhibit reduced inactivation (both VDI and CDI) resulting in prolonged Ca^{2+} entry that delays action potential repolarization and disrupts Ca^{2+} homeostasis (Barrett and Tsien, 2008; Dick et al., 2016; Calorio et al., 2019). As such, identifying mechanisms that reverse this change would be beneficial from the perspective of devising new therapeutics.

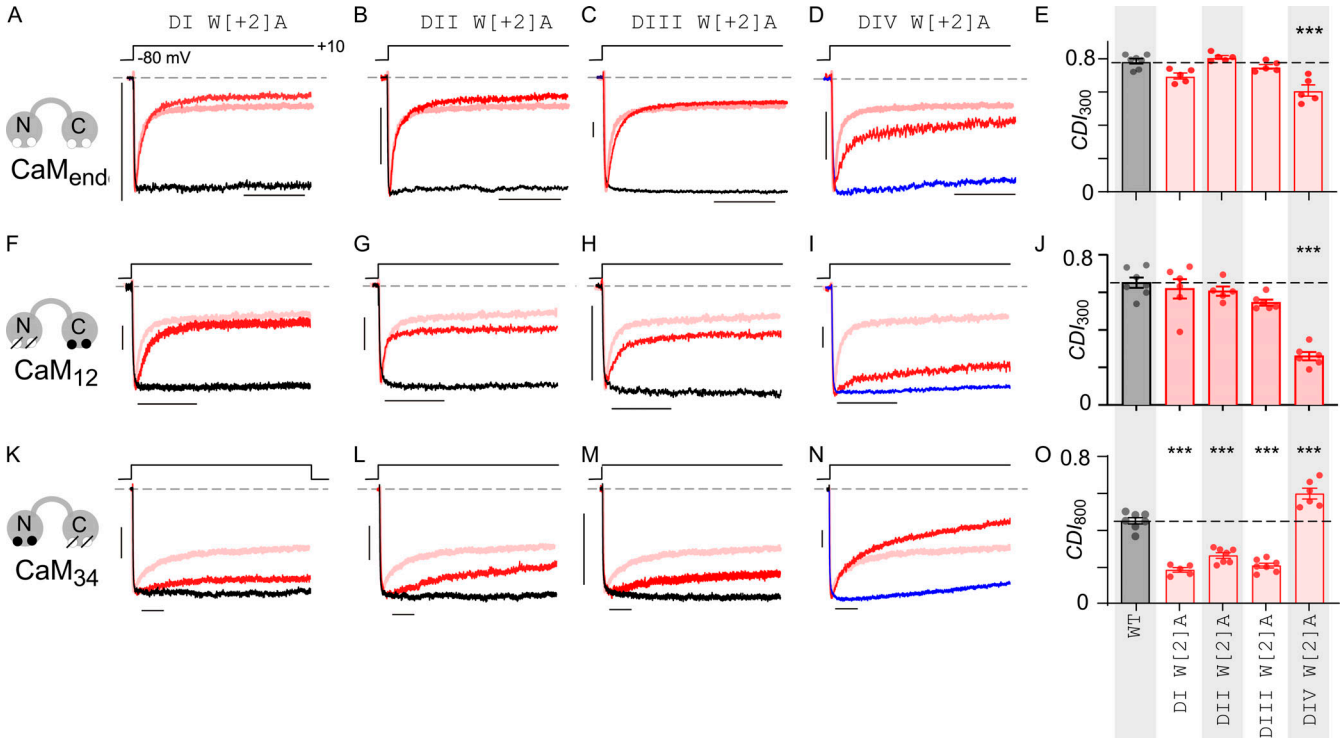

Figure 5. **Structural biparititioning of CDI mediated by distinct CaM lobes. (A)** Exemplar currents show strong CDI of DI W[+2]A mutation as evident from accelerated current decay observed with Ca^{2+} (red) versus Ba^{2+} (black) currents evoked in response to a 300-ms test pulse. Ca^{2+} current decay of wild-type $Ca_V1.3$ is shown as rose trace to facilitate comparison. Here, measurement obtained in the presence of endogenous CaM and therefore net CDI includes contributions of both N- and C-lobes of CaM. **(B and C)** DII W[+2]A and DIII W[+2]A mutations minimally perturb CDI. Format as in panel A. **(D)** $Ca_V1.3$ DIV W[+2]A mutation partially diminishes CDI. Here, CDI is measured by comparing inactivation in Ca^{2+} with endogenous CaM versus CaM_{1234} coexpressed (blue trace). **(E)** Population data confirms a mild reduction in CDI observed with W[+2]A mutation. $P < 0.001$ by Tukey's multiple comparisons test. Each bar and error, mean ± SEM. $n = 7$ cells for $Ca_V1.3$ wild-type and $n = 5$ for all mutant channels. **(F–J)** CDI mediated by the C-lobe of CaM is selectively diminished by $Ca_V1.3$ DIV W[+2]A mutation. Here, the component of C-lobe CDI is isolated by coexpression of CaM_{12}. For DIV W[+2]A mutant, we compared inactivation with CaM_{12} to CaM_{1234}. Red trace, Ca^{2+} current; black trace, Ba^{2+} current; rose trace, Ca^{2+} current from $Ca_V1.3$ WT co-expressed with CaM_{12}. Each bar and error, mean ± SEM. $n = 6$ cells ($Ca_V1.3$ wild-type), $n = 5$ cells (DI W[+2]A), $n = 5$ cells (DII W[+2]A), $n = 6$ cells (DIII W[+2]A), and $n = 7$ cells (DIV W[+2]A). ***$P < 0.001$ by Tukey's multiple comparisons test. **(K–O)** CDI mediated by N-lobe of CaM is diminished by $Ca_V1.3$ DI W[+2]A, DII W[+2]A, and DIII W[+2]A mutations. However, DIV W[+2]A increases N-lobe CDI. Here, N-lobe CDI is isolated by coexpression of CaM_{34}. Red trace, Ca^{2+} current; black trace, Ba^{2+} current; rose trace, Ca^{2+} current from $Ca_V1.3$ WT co-expressed with CaM_{34}. For DIV W[+2]A mutant, we compared inactivation with CaM_{34} versus when CaM_{1234} is coexpressed (blue trace). Each bar and error, mean ± SEM. $n = 5$ cells ($Ca_V1.3$ wild-type), $n = 7$ cells (DI W[+2]A), $n = 7$ cells (DII W[+2]A), $n = 6$ cells (DIII W[+2]A), and $n = 7$ cells (DIV W[+2]A). ***$P < 0.001$ by Tukey's multiple comparisons test.

Since DIV W[+2]A mutation in $Ca_V1.3$ enhanced VDI, we probed whether the analogous mutation in a TS $Ca_V1.2$ variant could reverse deficits in VDI observed for mutant channels. We considered the G406R variant, known to exhibit a strong functional phenotype. Consistent with previous studies (Barrett and Tsien, 2008; Dick et al., 2016), we found that this variant exhibited reduced both VDI and CDI compared with wild-type $Ca_V1.2$ channels (Fig. 6, A and B). Introduction of the DIV W[+2]A mutation to the G406 variant resulted in a marked enhancement in VDI (Fig. 6 C), restoring overall inactivation to near wild-type levels. This finding suggests that enhancing the conformational flexibility of the SF may be a potential approach to reverse the pathophysiological reduction in inactivation linked to TS.

Discussion

Ca_V channel inactivation is a physiologically consequential and mechanistically rich ion channel feedback regulation that serves to limit excess Ca^{2+} entry into neurons and cardiomyocytes (Minor and Findeisen, 2010; Ben-Johny and Yue, 2014). Here, we probed the functional importance of the SF in tuning both VDI and CDI. Mutagenesis of an ultrahighly conserved W[+2] residue (Payandeh and Minor, 2015) in DI–DIV revealed an unexpected asymmetric role of the pore domain in tuning channel inactivation. First, we found that mutating the W[+2] residue in DIV but not DI–DIII enhanced VDI. MD simulations showed that DIV W[+2]A mutation increased the local conformational flexibility of the pore domain, hinting at a distinct role for the SF gate in tuning VDI. Although the W[+2] residue is symmetric in all four domains, the asymmetric effect of mutating DIV W[+2] residue on VDI stems from distinct differences in neighboring residues that stabilize the interdomain interfaces. Second, an in-depth analysis of CDI revealed a structural bifurcation of CaM signaling, whereby the DIV mutation selectively diminished CDI mediated by the C-lobe of CaM, while mutations in DI–DIII preferentially reduced N-lobe CDI. Taken together, these findings demonstrate that the pseudotetrameric arrangement of the eukaryotic Ca_V channel pore enables asymmetric conformational

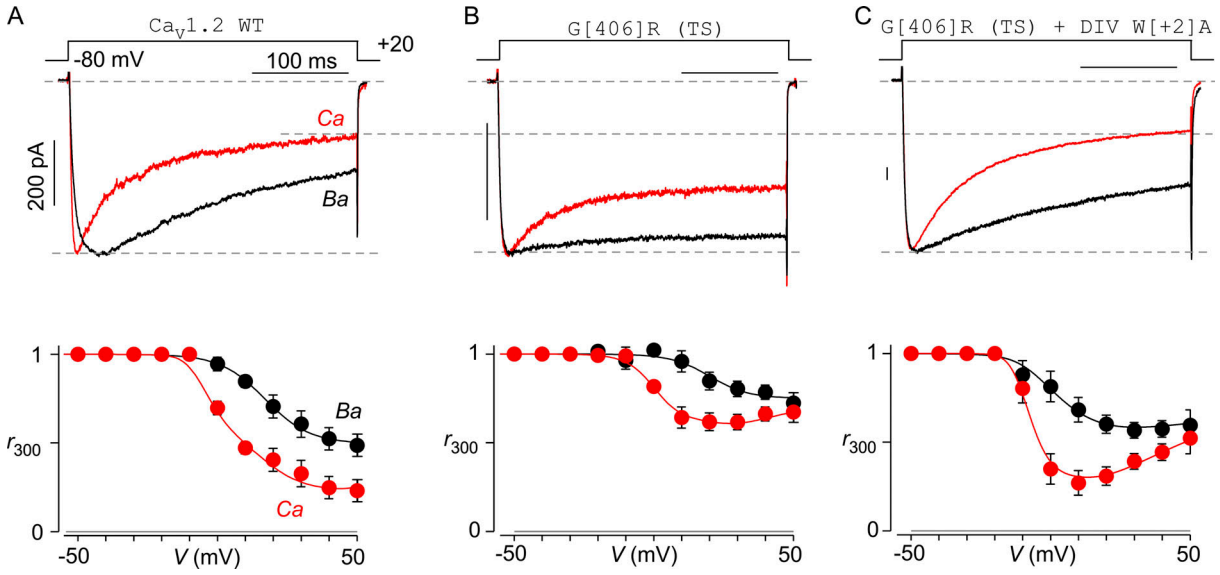

Figure 6. **SF domain mutation enhances inactivation of TS-associated $Ca_V1.2$ mutant channel. (A)** Top: Wild-type human $Ca_V1.2$ channel exhibits robust CDI and VDI. Black trace, Ba^{2+} current; red trace, Ca^{2+} current. Bottom: Population data show baseline inactivation of $Ca_V1.2$ measured as r_{300}, the fraction of peak current remaining following 300 ms, with either Ca^{2+} (red) or Ba^{2+} (black) as the charge carrier. Each symbol, mean ± SEM. n = 5 cells. **(B)** $Ca_V1.2$ G406R mutant linked to TS shows reduced VDI and CDI. Format as in panel A. n = 6 cells. **(C)** Introducing the DIV W[+2]A mutation on TS-linked CaV1.2 G406R background enhances VDI. This finding suggests that increasing the conformational flexibility of DIV SF may be a potential approach to reverse TS pathophysiology. n = 6 cells.

changes that are fundamentally important for its distinct inactivation mechanisms.

For VDI, a hinged-lid mechanism has been proposed based on multiple lines of evidence (Stotz et al., 2000; Dafi et al., 2004; Tadross et al., 2010): (1) chimeric analyses of $Ca_V1/2$ channels pointed to the involvement of both the DI S6 segment and the intracellular DI–DII linker in tuning inactivation kinetics (Stotz and Zamponi, 2001; Stotz et al., 2004). (2) Kinetics of VDI is dependent on the specific auxiliary $Ca_V\beta$ subunit associated with the channel DI–DII linker, with membrane-tethered $Ca_V\beta$ subunits slowing VDI (Olcese et al., 1994; Chien et al., 1996). (3) Mutagenesis of the presumed S6 transmembrane receptor site also alters VDI (Stotz and Zamponi, 2001; Dafi et al., 2004; Tadross et al., 2010). (4) Exogenous expression of DI–DII linker as a peptide accelerates VDI (Cens et al., 1999). Structurally, the DI–DII linker forms a continuous helix with the S6 gate and disruption of the helix by a polyglycine linker promotes VDI, findings that are inconsistent with a hinged-lid model (Findeisen and Minor, 2009; Wu et al., 2016). Recent studies instead point to the involvement of the SF for VDI of Ca_V channels, with select mutations in the SF diminishing VDI (Abderemane-Ali et al., 2019). In this study, the slow baseline VDI of $Ca_V1.3$ enabled us to discern the potential role of the SF using a gain-of-function approach by introducing mutations to upregulate VDI. Our results suggest that the SF interface between DIII and DIV may be a previously unrecognized locus for VDI. Although the W[+2] residue is symmetrically present in all four domains, only the DIV W[+2]A mutation increased local conformational flexibility and enhanced VDI. Further mutagenesis of this residue showed that the kinetics of VDI varied depending on the bulkiness of the residue at the DIV [+2] position, with bulkier residues slowing inactivation kinetics. This asymmetric effect of the DIV mutation reflects distinct differences in residues at the DIII–DIV interdomain interface (Fig. 7 A). Specifically, the W[+2] residue interacts with a T[−2] residue that is present in all four domains. Beyond this, the DI–DII, DII–DII, and DIV–DI interdomain interfaces are also stabilized by additional interactions between either a Q[−5] or R[−5] and a Y[+7] residue from the neighboring domain. However, this additional stabilizing interaction is absent in the DIII–DIV interface, with a T[−5] in the DIII and an L[+7] in the DIV locations. Consequently, the DIV W[+2]A mutation destabilizes the SF conformation. Consistent with this possibility, the DIV W[+2]A/DIII T[−5]Q double mutation partially reversed the increase in VDI. Taken together, the interdomain interaction of DIV W[+2] with neighboring residues may be envisioned as a brake that stabilizes the SF conformation allowing sustained ion influx during prolonged depolarization.

For $Ca_V1.3$, mutating residues in the distal S6 domain below the bundle crossing have also been shown to enhance VDI (Tadross et al., 2010). However, this form of VDI exhibited a conventional Boltzmann-shaped voltage dependence and its magnitude was susceptible to further modulation by $Ca_V\beta$ subunits. By contrast, VDI uncovered by SF mutations exhibited an atypical U-shaped voltage dependence and was insensitive to modulation by the $Ca_V\beta$ subunits. Mechanistically, this feature of SF-dependent inactivation may reflect its dependence on pore occupancy by the permeant ion, which may be reduced at higher voltages owing to a reduced driving force. Nonetheless, the disparate functional signatures suggest that the two forms of VDI are distinct. Interestingly, $Ca_V2.2$ channels have been shown to also undergo preferential intermediate closed-state

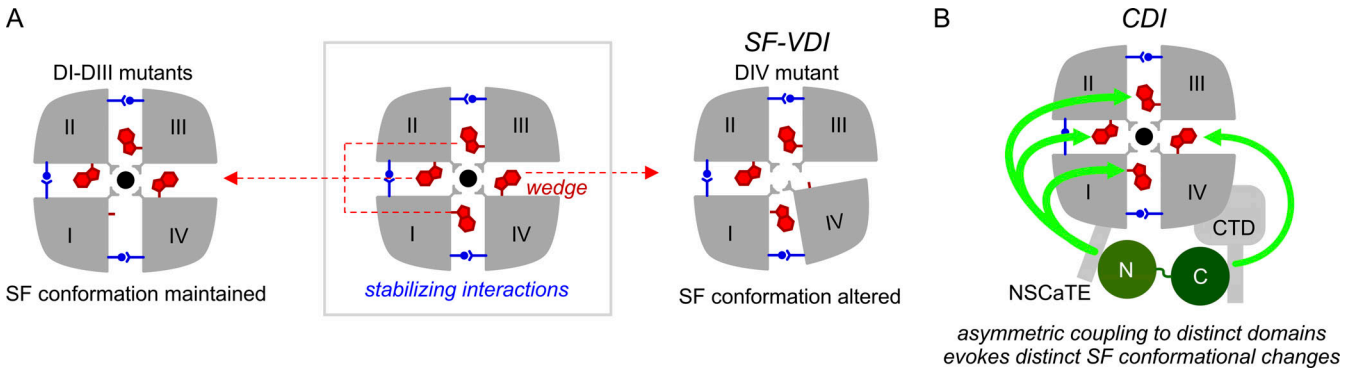

Figure 7. **Asymmetric effect of SF mutations on $Ca_V1.3$ VDI and CDI. (A)** Schematic shows asymmetric effect of the SF W[+2]A mutations in evoking VDI of $Ca_V1.3$. The interdomain interface between DIII and DIV is stabilized primarily by the conserved W[+2] residue which may serve as a wedge. Disruption of this interaction destabilizes the local conformation. By contrast, the interdomain interface between DI–DII, DII–DII, and DI–DIV is stabilized by both the W[+2] residue and through additional interdomain contacts. Consequently, SF conformation is maintained even with the W[+2]A mutation in DI through DIII. **(B)** For CDI, the W[+2] residue likely plays a role in transducing SF conformational rearrangements. The N- versus C-lobe of CaM appears to be asymmetrically coupled to distinct SF domains, likely evoking distinct SF conformational changes.

inactivation with a similar U-shaped voltage dependence (Patil et al., 1998). Recent cryo-EM studies identified a cytosolic helical segment known as W-helix unique to Ca_V2 DII–DIII linker that occludes the ion conduction pathway (Dong et al., 2021; Gao et al., 2021). Either deletion or disruption of this domain by alternative splicing was shown to diminish preferential intermediate closed-state inactivation (Dong et al., 2021). It is possible that altered conformational changes in the SF of $Ca_V2.2$ may also contribute to this process.

CDI is initiated by CaM-dependent conformational changes in the cytosolic domain of Ca_V channels (Budde et al., 2002; Halling et al., 2005; Minor and Findeisen, 2010; Ben Johny and Yue, 2015). Ca^{2+} binding to the individual N- and C-lobes of CaM can trigger distinct forms of channel regulation (Lee et al., 2000; DeMaria et al., 2001; Liang et al., 2003), a phenomenon known as "functional bipartition" of CaM (Kink et al., 1990; Saimi and Kung, 1994). For $Ca_V1.3$, the N- and C-lobe of CaM evoke kinetically distinct forms of inactivation (Yang et al., 2006; Dick et al., 2008). Molecularly, these effects are initiated by a Ca^{2+}-dependent switching of CaM interaction with distinct channel interfaces–the Ca^{2+}-bound N-lobe engages the *NSCaTE* domain on the channel amino-terminus (Dick et al., 2008; Simms et al., 2013), while the C-lobe associates with the C-terminus and evokes a conformational change (Kim et al., 2004; Black et al., 2005; Van Petegem et al., 2005; Asmara et al., 2010; Ben-Johny et al., 2013; Banerjee et al., 2018). How these disparate changes in the cytosolic domains are coupled to the pore domain is not fully understood. Two end-stage mechanisms of CDI have been proposed: (1) an allosteric change in the activation gate corresponding to a change in modal gating (Tadross et al., 2010) or (2) an altered selectivity filter conformation (Abderemane-Ali et al., 2019). First, single-channel recordings show that Ca^{2+}/CaM regulation switches channels from a high-activity gating with "flickery" openings to a low-activity gating mode with "sparse" openings (Imredy and Yue, 1994). Furthermore, both engineered and human disease-linked mutations in the S6 gate that enhance channel activation proportionately weaken CDI, all consistent with an allosteric mechanism (Tadross et al., 2010). Second, $Ca_V1.2$ inactivation is sensitive to extracellular Ca^{2+} and CDI alters the propensity for pore blockade by Gd^{3+}, suggesting an involvement of the SF (Babich et al., 2005, 2007). More concretely, mutations in the SF alter CDI. Specifically, SF DII D[+1]A diminishes CDI of various $Ca_V1/2$ channels without any apparent effect on VDI (Abderemane-Ali et al., 2019). Our present findings further corroborate the essential role of the SF in mediating CDI and uncover an unexpected asymmetry in this process. The DIV W[+2]A mutation that destabilizes the SF, evokes contrasting effects on CDI mediated by distinct CaM lobes (Fig. 7 B). While this mutation enhances N-lobe CDI, it also suppresses C-lobe CDI. By contrast, mutating corresponding W[+2] residues in DI–DIII revealed a selective effect on N-lobe CDI but not C-lobe CDI. This divergent effect suggests that the specific interdomain interactions of the W[+2] residue in the SF may be involved in the transduction of cytosolic conformational changes to the end-stage mechanism. Of note, MD simulations did not show a marked increase in conformational flexibility with DI–DIII W[+2]A mutations. However, these simulations did not include the channel C- and N-terminal domains, which are essential for CaM regulation. It is possible that CaM rearrangement in the cytosolic domains may evoke additional changes in the SF domain. These findings also suggest that there may be distinct SF conformational changes associated with N- versus C-lobe CDI. How does one reconcile an allosteric mechanism evident from single-channel studies with a change in SF conformation? One possibility emerges from studies of Kcsa channels where altered SF conformation has been shown to result in shifts in modal gating (Chakrapani et al., 2011). The activation gate of these channels is also coupled to the SF gate (Cuello et al., 2010; Heer et al., 2017), suggesting that the two mechanisms may overlap. Similar findings have also been reported with other ion channels (Boiteux et al., 2014; Kopec et al., 2019; Coonen et al., 2020).

From a pathophysiological perspective, channelopathic mutations in both $Ca_V1.2$ and $Ca_V1.3$ are known to reduce both VDI and CDI (Dick et al., 2016; Ortner et al., 2020; Bamgboye et al., 2022a). This deficit in inactivation is thought to result in sustained Ca^{2+} influx that is proarrhythmic. From a pharmacological

perspective, traditional small molecule blockers of Ca_V1 channels have been largely inadequate as a therapy. First, mutant channels often exhibit a reduced affinity for many small molecule blockers (Bamgboye et al., 2022b). Second, small molecule Ca_V1 inhibitors impact the peak Ca^{2+} current, which in turn inhibits the overall Ca^{2+} influx causing adverse negative inotropic effects (Angelini et al., 2021). Instead, Ca_V1 gating modifiers that enhance inactivation have been proposed as a new and potentially more effective class of antiarrhythmic drugs (Angelini et al., 2021). In this study, we found that the introduction of the DIV W[+2]A mutation can in fact enhance the VDI of TS-linked mutant channels and restore overall inactivation to near wild-type levels. This increase in VDI points to the possibility that there may be a coupling between S6 gate and the SF region. Of note, we did not observe a significant reduction in overall CDI here with the SF mutation, as these experiments were conducted with endogenous CaM with both lobes intact. This is consistent with results in $Ca_V1.3$ where N-lobe CDI is enhanced even as C-lobe CDI is reduced resulting in only a modest reduction in CDI in the presence of endogenous CaM. Altogether, this finding suggests that either destabilizing or increasing the conformational flexibility of the DIV SF domain may suffice to upregulate Ca_V1 inactivation and potentially reverse some of the pathophysiology linked to TS.

Of broader relevance, the W[+2] residue is highly conserved across eukaryotic Ca_V, Na_V, and NALCN leak channels, as well as prokaryotic $BacNa_V$, suggesting that asymmetric SF conformational changes may constitute an ancient and general mechanism for channel inactivation (Payandeh and Minor, 2015). For $Na_V1.4$, the DI W[+2]C mutation was shown to inhibit slow inactivation while mutations of analogous residues in DII–DIV had minimal effect (Balser et al., 1996). In like manner, mutating the DIV A[0] residue that forms part of the SF of $Na_V1.4$ introduces an ultraslow component of inactivation with a U-shaped voltage-dependence, much like the $Ca_V1.3$ DIV W[+2]A mutation (Todt et al., 1999). For the homotetrameric bacterial Na_V channels, asymmetric pore collapse is thought to be the underlying structural mechanism for inactivation (Pavlov et al., 2005; Payandeh et al., 2012). The W[+2] residue serves as an important anchor for the SF that allows hydrogen bonding interactions with T[−2] residues of neighboring subunits (Payandeh and Minor, 2015). This interaction has been proposed to be important to allow SF conformational changes to be influenced by neighboring subunits (Payandeh and Minor, 2015). Structurally, the slow inactivation of $BacNa_V$ channels increases the conformational flexibility of the selectivity filter, resulting in a reorientation of the pore helices that change the intersubunit cavity volumes and accessibility of lipids (Chatterjee et al., 2018).

Overall, this study furnishes new insights into the role of the SF in VDI and CDI of $Ca_V1.3$ and it uncovers how asymmetric changes in the SF allow structural bifurcation of CaM signaling, a scheme that may be broadly relevant (Saimi and Kung, 2002; Liang et al., 2003; Ben-Johny et al., 2014).

Data availability

All data are available in the article itself or in the supplementary materials.

Acknowledgments

Crina M. Nimigean served as editor.

We thank Dr. Ryan Mahling, Dr. Nourdine Chakouri, Dr. Ivy Dick, Dr. Po Wei Kang, and Dr. Filip van Petegem for their helpful feedback.

This study is supported by funding from the National Institute of Neurological Disorders and Stroke (R01 NS110672) to M. Ben-Johny, American Heart Association Predoctoral Fellowship (award ID 835091) to P.J. del Rivero Morfin, a grant from the Austrian Science Fund (FWF) P35618 to B.E. Flucher, and Austrian Academy of sciences APART-MINT postdoctoral fellowship to M.L.I. Fernández-Quintero and the Austrian Science fund (P34514). The content is solely the responsibility of the authors and does not necessarily represent the official views of the National Institutes of Health or the American Heart Association. The computational results presented here have been achieved in part using the Vienna Scientific Cluster (VSC). We thank PRACE for awarding us access to Piz Daint at CSCS, Switzerland.

Author contributions: P.J. del Rivero Morfin, M.L.I. Fernández-Quintero, K.R. Liedl, B.E. Flucher, and M. Ben-Johny designed research, P.J. del Rivero Morfin, M.L.I. Fernández-Quintero, A.L. Kochiss, and M. Ben-Johny performed research, acquired and analyzed data, P.J. del Rivero Morfin, M.L.I. Fernández-Quintero, K.R. Liedl, B.E. Flucher, and M. Ben-Johny contributed new reagents/analytic tools; M. Ben-Johny, M.L.I. Fernández-Quintero, and B.E. Flucher funding acquisition; P.J. del Rivero Morfin, M.L.I. Fernández-Quintero, B.E. Flucher, and M. Ben-Johny made figures and wrote the original draft; and all authors revised the manuscript.

Disclosures: The authors declare no competing interests exist.

Submitted: 1 February 2023
Revised: 8 October 2023
Revised: 16 November 2023
Accepted: 14 December 2023

References

Abderemane-Ali, F., F. Findeisen, N.D. Rossen, and D.L. Minor Jr. 2019. A selectivity filter gate controls voltage-gated calcium channel calcium-dependent inactivation. *Neuron.* 101:1134–1149.e3. https://doi.org/10.1016/j.neuron.2019.01.011

Angelini, M., A. Pezhouman, N. Savalli, M.G. Chang, F. Steccanella, K. Scranton, G. Calmettes, M. Ottolia, A. Pantazis, H.S. Karagueuzian, et al. 2021. Suppression of ventricular arrhythmias by targeting late L-type Ca^{2+} current. *J. Gen. Physiol.* 153:e202212584. https://doi.org/10.1085/jgp.202012584

Asmara, H., E. Minobe, Z.A. Saud, and M. Kameyama. 2010. Interactions of calmodulin with the multiple binding sites of Cav1.2 Ca^{2+} channels. *J. Pharmacol. Sci.* 112:397–404. https://doi.org/10.1254/jphs.09342FP

Babich, O., D. Isaev, and R. Shirokov. 2005. Role of extracellular Ca^{2+} in gating of CaV1.2 channels. *J. Physiol.* 565:709–715. https://doi.org/10.1113/jphysiol.2005.086561

Babich, O., V. Matveev, A.L. Harris, and R. Shirokov. 2007. Ca^{2+}-dependent inactivation of CaV1.2 channels prevents Gd3+ block: Does Ca^{2+} block the pore of inactivated channels? *J. Gen. Physiol.* 129:477–483. https://doi.org/10.1085/jgp.200709734

Balser, J.R., H.B. Nuss, N. Chiamvimonvat, M.T. Pérez-García, E. Marban, and G.F. Tomaselli. 1996. External pore residue mediates slow inactivation in mu 1 rat skeletal muscle sodium channels. *J. Physiol.* 494:431–442. https://doi.org/10.1113/jphysiol.1996.sp021503

Bamgboye, M.A., K.G. Herold, D.C.O. Vieira, M.K. Traficante, P.J. Rogers, M. Ben-Johny, and I.E. Dick. 2022a. CaV1.2 channelopathic mutations evoke diverse pathophysiological mechanisms. *J. Gen. Physiol.* 154: e202213209. https://doi.org/10.1085/jgp.202213209

Bamgboye, M.A., M.K. Traficante, J. Owoyemi, D. DiSilvestre, D.C.O. Vieira, and I.E. Dick. 2022b. Impaired $Ca_V1.2$ inactivation reduces the efficacy of calcium channel blockers in the treatment of LQT8. *J. Mol. Cell. Cardiol.* 173:92–100. https://doi.org/10.1016/j.yjmcc.2022.10.003

Banerjee, R., J.B. Yoder, D.T. Yue, L.M. Amzel, G.F. Tomaselli, S.B. Gabelli, and M. Ben-Johny. 2018. Bilobal architecture is a requirement for calmodulin signaling to $Ca_V1.3$ channels. *Proc. Natl. Acad. Sci. USA.* 115: E3026–E3035. https://doi.org/10.1073/pnas.1716381115

Barrett, C.F., and R.W. Tsien. 2008. The Timothy syndrome mutation differentially affects voltage- and calcium-dependent inactivation of CaV1.2 L-type calcium channels. *Proc. Natl. Acad. Sci. USA.* 105: 2157–2162. https://doi.org/10.1073/pnas.0710501105

Ben Johny, M., P.S. Yang, H. Bazzazi, and D.T. Yue. 2013. Dynamic switching of calmodulin interactions underlies Ca^{2+} regulation of CaV1.3 channels. *Nat. Commun.* 4:1717. https://doi.org/10.1038/ncomms2727

Ben-Johny, M., P.S. Yang, J. Niu, W. Yang, R. Joshi-Mukherjee, and D.T. Yue. 2014. Conservation of Ca^{2+}/calmodulin regulation across Na and Ca^{2+} channels. *Cell.* 157:1657–1670. https://doi.org/10.1016/j.cell.2014.04.035

Ben-Johny, M., and D.T. Yue. 2014. Calmodulin regulation (calmodulation) of voltage-gated calcium channels. *J. Gen. Physiol.* 143:679–692. https://doi.org/10.1085/jgp.201311153

Ben Johny, M., and D.T. Yue. 2015. Calmodulin regulation of voltage-gated calcium channels and beyond. In Handbook of Ion Channels. M. Trudeau and J. Zheng, editors. CRC Press, Boca Raton, FL.

Berridge, M.J., P. Lipp, and M.D. Bootman. 2000. The versatility and universality of calcium signalling. *Nat. Rev. Mol. Cell Biol.* 1:11–21. https://doi.org/10.1038/35036035

Bers, D.M. 2002. Cardiac excitation-contraction coupling. *Nature.* 415: 198–205. https://doi.org/10.1038/415198a

Black, D.J., D.B. Halling, D.V. Mandich, S.E. Pedersen, R.A. Altschuld, and S.L. Hamilton. 2005. Calmodulin interactions with IQ peptides from voltage-dependent calcium channels. *Am. J. Physiol. Cell Physiol.* 288: C669–C676. https://doi.org/10.1152/ajpcell.00191.2004

Boiteux, C., I. Vorobyov, and T.W. Allen. 2014. Ion conduction and conformational flexibility of a bacterial voltage-gated sodium channel. *Proc. Natl. Acad. Sci. USA.* 111:3454–3459. https://doi.org/10.1073/pnas.1320907111

Budde, T., S. Meuth, and H.C. Pape. 2002. Calcium-dependent inactivation of neuronal calcium channels. *Nat. Rev. Neurosci.* 3:873–883. https://doi.org/10.1038/nrn959

Calorio, C., D. Gavello, L. Guarina, C. Salio, M. Sassoè-Pognetto, C. Riganti, F.T. Bianchi, N.T. Hofer, P. Tuluc, G.J. Obermair, et al. 2019. Impaired chromaffin cell excitability and exocytosis in autistic Timothy syndrome TS2-neo mouse rescued by L-type calcium channel blockers. *J. Physiol.* 597:1705–1733. https://doi.org/10.1113/JP277487

Catterall, W.A., G. Wisedchaisri, and N. Zheng. 2017. The chemical basis for electrical signaling. *Nat. Chem. Biol.* 13:455–463. https://doi.org/10.1038/nchembio.2353

Cens, T., S. Restituito, S. Galas, and P. Charnet. 1999. Voltage and calcium use the same molecular determinants to inactivate calcium channels. *J. Biol. Chem.* 274:5483–5490. https://doi.org/10.1074/jbc.274.9.5483

Chakrapani, S., J.F. Cordero-Morales, V. Jogini, A.C. Pan, D.M. Cortes, B. Roux, and E. Perozo. 2011. On the structural basis of modal gating behavior in K(+) channels. *Nat. Struct. Mol. Biol.* 18:67–74. https://doi.org/10.1038/nsmb.1968

Chao, S.H., Y. Suzuki, J.R. Zysk, and W.Y. Cheung. 1984. Activation of calmodulin by various metal cations as a function of ionic radius. *Mol. Pharmacol.* 26:75–82.

Chatterjee, S., R. Vyas, S.V. Chalamalasetti, I.D. Sahu, J. Clatot, X. Wan, G.A. Lorigan, I. Deschênes, and S. Chakrapani. 2018. The voltage-gated sodium channel pore exhibits conformational flexibility during slow inactivation. *J. Gen. Physiol.* 150:1333–1347. https://doi.org/10.1085/jgp.201812118

Chien, A.J., K.M. Carr, R.E. Shirokov, E. Rios, and M.M. Hosey. 1996. Identification of palmitoylation sites within the L-type calcium channel beta2a subunit and effects on channel function. *J. Biol. Chem.* 271: 26465–26468. https://doi.org/10.1074/jbc.271.43.26465

Colecraft, H.M., B. Alseikhan, S.X. Takahashi, D. Chaudhuri, S. Mittman, V. Yegnasubramanian, R.S. Alvania, D.C. Johns, E. Marbán, and D.T. Yue. 2002. Novel functional properties of Ca(2+) channel beta subunits revealed by their expression in adult rat heart cells. *J. Physiol.* 541: 435–452. https://doi.org/10.1113/jphysiol.2002.018515

Coonen, L., E. Mayeur, N. De Neuter, D.J. Snyders, L.G. Cuello, and A.J. Labro. 2020. The selectivity filter is involved in the U-type inactivation process of Kv2.1 and Kv3.1 channels. *Biophys. J.* 118:2612–2620. https://doi.org/10.1016/j.bpj.2020.03.032

Cuello, L.G., V. Jogini, D.M. Cortes, A.C. Pan, D.G. Gagnon, O. Dalmas, J.F. Cordero-Morales, S. Chakrapani, B. Roux, and E. Perozo. 2010. Structural basis for the coupling between activation and inactivation gates in K(+) channels. *Nature.* 466:272–275. https://doi.org/10.1038/nature09136

Dafi, O., L. Berrou, Y. Dodier, A. Raybaud, R. Sauvé, and L. Parent. 2004. Negatively charged residues in the N-terminal of the AID helix confer slow voltage dependent inactivation gating to CaV1.2. *Biophys. J.* 87: 3181–3192. https://doi.org/10.1529/biophysj.104.045559

DeMaria, C.D., T.W. Soong, B.A. Alseikhan, R.S. Alvania, and D.T. Yue. 2001. Calmodulin bifurcates the local Ca^{2+} signal that modulates P/Q-type Ca^{2+} channels. *Nature.* 411:484–489. https://doi.org/10.1038/35078091

Dick, I.E., R. Joshi-Mukherjee, W. Yang, and D.T. Yue. 2012. Nonlinear threshold behavior in the induction of arryhthmias by channels bearing Timothy Syndrome mutations (abstr.). *Biophys. J.* 102:542a. https://doi.org/10.1016/j.bpj.2011.11.2958

Dick, I.E., R. Joshi-Mukherjee, W. Yang, and D.T. Yue. 2016. Arrhythmogenesis in Timothy Syndrome is associated with defects in Ca(2+)-dependent inactivation. *Nat. Commun.* 7:10370. https://doi.org/10.1038/ncomms10370

Dick, I.E., M.R. Tadross, H. Liang, L.H. Tay, W. Yang, and D.T. Yue. 2008. A modular switch for spatial Ca^{2+} selectivity in the calmodulin regulation of CaV channels. *Nature.* 451:830–834. https://doi.org/10.1038/nature06529

Dickson, C.J., B.D. Madej, A.A. Skjevik, R.M. Betz, K. Teigen, I.R. Gould, and R.C. Walker. 2014. Lipid14: The amber lipid force field. *J. Chem. Theor. Comput.* 10:865–879. https://doi.org/10.1021/ct4010307

Dolmetsch, R. 2003. Excitation-transcription coupling: Signaling by ion channels to the nucleus. *Sci. STKE.* 2003:PE4. https://doi.org/10.1126/stke.2003.166.pe4

Dong, Y., Y. Gao, S. Xu, Y. Wang, Z. Yu, Y. Li, B. Li, T. Yuan, B. Yang, X.C. Zhang, et al. 2021. Closed-state inactivation and pore-blocker modulation mechanisms of human $Ca_V2.2$. *Cell Rep.* 37:109931. https://doi.org/10.1016/j.celrep.2021.109931

Fernández-Quintero, M.L., Y. El Ghaleb, P. Tuluc, M. Campiglio, K.R. Liedl, and B.E. Flucher. 2021. Structural determinants of voltage-gating properties in calcium channels. *Elife.* 10:e64087. https://doi.org/10.7554/eLife.64087

Findeisen, F., and D.L. Minor Jr. 2009. Disruption of the IS6-AID linker affects voltage-gated calcium channel inactivation and facilitation. *J. Gen. Physiol.* 133:327–343. https://doi.org/10.1085/jgp.200810143

Gao, S., X. Yao, and N. Yan. 2021. Structure of human $Ca_v2.2$ channel blocked by the painkiller ziconotide. *Nature.* 596:143–147. https://doi.org/10.1038/s41586-021-03699-6

Goldschen-Ohm, M.P., D.L. Capes, K.M. Oelstrom, and B. Chanda. 2013. Multiple pore conformations driven by asynchronous movements of voltage sensors in a eukaryotic sodium channel. *Nat. Commun.* 4:1350. https://doi.org/10.1038/ncomms2356

Halling, D.B., P. Aracena-Parks, and S.L. Hamilton. 2005. Regulation of voltage-gated Ca^{2+} channels by calmodulin. *Sci. STKE.* 2005:re15. https://doi.org/10.1126/stke.3152005re15

He, L.L., Y. Zhang, Y.H. Chen, Y. Yamada, and J. Yang. 2007. Functional modularity of the beta-subunit of voltage-gated Ca^{2+} channels. *Biophys. J.* 93:834–845. https://doi.org/10.1529/biophysj.106.101691

Heer, F.T., D.J. Posson, W. Wojtas-Niziurski, C.M. Nimigean, and S. Bernèche. 2017. Mechanism of activation at the selectivity filter of the KcsA K^+ channel. *Elife.* 6:e25844. https://doi.org/10.7554/eLife.25844

Hoshi, T., W.N. Zagotta, and R.W. Aldrich. 1990. Biophysical and molecular mechanisms of Shaker potassium channel inactivation. *Science.* 250: 533–538. https://doi.org/10.1126/science.2122519

Hoshi, T., W.N. Zagotta, and R.W. Aldrich. 1991. Two types of inactivation in shaker K^+ channels: Effects of alterations in the carboxy-terminal region. *Neuron.* 7:547–556. https://doi.org/10.1016/0896-6273(91)90367-9

Imredy, J.P., and D.T. Yue. 1994. Mechanism of Ca(2+)-sensitive inactivation of L-type Ca^{2+} channels. *Neuron.* 12:1301–1318. https://doi.org/10.1016/0896-6273(94)90446-4

Jo, S., T. Kim, V.G. Iyer, and W. Im. 2008. CHARMM-GUI: A web-based graphical user interface for CHARMM. *J. Comput. Chem.* 29:1859–1865. https://doi.org/10.1002/jcc.20945

Jo, S., J.B. Lim, J.B. Klauda, and W. Im. 2009. CHARMM-GUI membrane builder for mixed bilayers and its application to yeast membranes. *Biophys. J.* 97:50–58. https://doi.org/10.1016/j.bpj.2009.04.013

Kim, J., S. Ghosh, D.A. Nunziato, and G.S. Pitt. 2004. Identification of the components controlling inactivation of voltage-gated Ca^{2+} channels. *Neuron*. 41:745–754. https://doi.org/10.1016/S0896-6273(04)00081-9

Kink, J.A., M.E. Maley, R.R. Preston, K.Y. Ling, M.A. Wallen-Friedman, Y. Saimi, and C. Kung. 1990. Mutations in paramecium calmodulin indicate functional differences between the C-terminal and N-terminal lobes in vivo. *Cell*. 62:165–174. https://doi.org/10.1016/0092-8674(90)90250-I

Kopec, W., B.S. Rothberg, and B.L. de Groot. 2019. Molecular mechanism of a potassium channel gating through activation gate-selectivity filter coupling. *Nat. Commun.* 10:5366. https://doi.org/10.1038/s41467-019-13227-w

Lee, A., T. Scheuer, and W.A. Catterall. 2000. Ca^{2+}/calmodulin-dependent facilitation and inactivation of P/Q-type Ca^{2+} channels. *J. Neurosci.* 20:6830–6838. https://doi.org/10.1523/JNEUROSCI.20-18-06830.2000

Liang, H., C.D. DeMaria, M.G. Erickson, M.X. Mori, B.A. Alseikhan, and D.T. Yue. 2003. Unified mechanisms of Ca^{2+} regulation across the Ca^{2+} channel family. *Neuron*. 39:951–960. https://doi.org/10.1016/S0896-6273(03)00560-9

Limpitikul, W.B., I.E. Dick, R. Joshi-Mukherjee, M.T. Overgaard, A.L. George Jr., and D.T. Yue. 2014. Calmodulin mutations associated with long QT syndrome prevent inactivation of cardiac L-type Ca(2+) currents and promote proarrhythmic behavior in ventricular myocytes. *J. Mol. Cell. Cardiol.* 74:115–124. https://doi.org/10.1016/j.yjmcc.2014.04.022

Minor, D.L. Jr., and F. Findeisen. 2010. Progress in the structural understanding of voltage-gated calcium channel (CaV) function and modulation. *Channels*. 4:459–474. https://doi.org/10.4161/chan.4.6.12867

Olcese, R., N. Qin, T. Schneider, A. Neely, X. Wei, E. Stefani, and L. Birnbaumer. 1994. The amino terminus of a calcium channel beta subunit sets rates of channel inactivation independently of the subunit's effect on activation. *Neuron*. 13:1433–1438. https://doi.org/10.1016/0896-6273(94)90428-6

Ortner, N.J., T. Kaserer, J.N. Copeland, and J. Striessnig. 2020. De novo CACNA1D Ca^{2+} channelopathies: Clinical phenotypes and molecular mechanism. *Pflugers Arch.* 472:755–773. https://doi.org/10.1007/s00424-020-02418-w

Patil, P.G., D.L. Brody, and D.T. Yue. 1998. Preferential closed-state inactivation of neuronal calcium channels. *Neuron*. 20:1027–1038. https://doi.org/10.1016/S0896-6273(00)80483-3

Pavlov, E., C. Bladen, R. Winkfein, C. Diao, P. Dhaliwal, and R.J. French. 2005. The pore, not cytoplasmic domains, underlies inactivation in a prokaryotic sodium channel. *Biophys. J.* 89:232–242. https://doi.org/10.1529/biophysj.104.056994

Payandeh, J., T.M. Gamal El-Din, T. Scheuer, N. Zheng, and W.A. Catterall. 2012. Crystal structure of a voltage-gated sodium channel in two potentially inactivated states. *Nature*. 486:135–139. https://doi.org/10.1038/nature11077

Payandeh, J., and D.L. Minor Jr. 2015. Bacterial voltage-gated sodium channels (BacNa(V)s) from the soil, sea, and salt lakes enlighten molecular mechanisms of electrical signaling and pharmacology in the brain and heart. *J. Mol. Biol.* 427:3–30. https://doi.org/10.1016/j.jmb.2014.08.010

Peterson, B.Z., C.D. DeMaria, J.P. Adelman, and D.T. Yue. 1999. Calmodulin is the Ca^{2+} sensor for Ca^{2+} -dependent inactivation of L-type calcium channels. *Neuron*. 22:549–558. https://doi.org/10.1016/S0896-6273(00)80709-6

Pinggera, A., A. Lieb, B. Benedetti, M. Lampert, S. Monteleone, K.R. Liedl, P. Tuluc, and J. Striessnig. 2015. CACNA1D de novo mutations in autism spectrum disorders activate Cav1.3 L-type calcium channels. *Biol. Psychiatry*. 77:816–822. https://doi.org/10.1016/j.biopsych.2014.11.020

Qin, N., R. Olcese, M. Bransby, T. Lin, and L. Birnbaumer. 1999. Ca^{2+}-induced inhibition of the cardiac Ca^{2+} channel depends on calmodulin. *Proc. Natl. Acad. Sci. USA*. 96:2435–2438. https://doi.org/10.1073/pnas.96.5.2435

Saimi, Y., and C. Kung. 1994. Ion channel regulation by calmodulin binding. *FEBS Lett.* 350:155–158. https://doi.org/10.1016/0014-5793(94)00782-9

Saimi, Y., and C. Kung. 2002. Calmodulin as an ion channel subunit. *Annu. Rev. Physiol.* 64:289–311. https://doi.org/10.1146/annurev.physiol.64.100301.111649

Savalli, N., M. Angelini, F. Steccanella, J. Wier, F. Wu, M. Quinonez, M. DiFranco, A. Neely, S.C. Cannon, and R. Olcese. 2021. The distinct role of the four voltage sensors of the skeletal CaV1.1 channel in voltage-dependent activation. *J. Gen. Physiol.* 153:153. https://doi.org/10.1085/jgp.202112915

Simms, B.A., I.A. Souza, and G.W. Zamponi. 2013. A novel calmodulin site in the Cav1.2 N-terminus regulates calcium-dependent inactivation. *Pflugers Arch.* 466:1793-1803. https://doi.org/10.1007/s00424-013-1423-9

Splawski, I., K.W. Timothy, L.M. Sharpe, N. Decher, P. Kumar, R. Bloise, C. Napolitano, P.J. Schwartz, R.M. Joseph, K. Condouris, et al. 2004. Ca(V)1.2 calcium channel dysfunction causes a multisystem disorder including arrhythmia and autism. *Cell*. 119:19–31. https://doi.org/10.1016/j.cell.2004.09.011

Stotz, S.C., J. Hamid, R.L. Spaetgens, S.E. Jarvis, and G.W. Zamponi. 2000. Fast inactivation of voltage-dependent calcium channels. A hinged-lid mechanism? *J. Biol. Chem.* 275:24575–24582. https://doi.org/10.1074/jbc.M000399200

Stotz, S.C., S.E. Jarvis, and G.W. Zamponi. 2004. Functional roles of cytoplasmic loops and pore lining transmembrane helices in the voltage-dependent inactivation of HVA calcium channels. *J. Physiol.* 554:263–273. https://doi.org/10.1113/jphysiol.2003.047068

Stotz, S.C., and G.W. Zamponi. 2001. Identification of inactivation determinants in the domain IIS6 region of high voltage-activated calcium channels. *J. Biol. Chem.* 276:33001–33010. https://doi.org/10.1074/jbc.M104387200

Tadross, M.R., M. Ben Johny, and D.T. Yue. 2010. Molecular endpoints of Ca^{2+}/calmodulin- and voltage-dependent inactivation of Ca(v)1.3 channels. *J. Gen. Physiol.* 135:197–215. https://doi.org/10.1085/jgp.200910308

Tadross, M.R., I.E. Dick, and D.T. Yue. 2008. Mechanism of local and global Ca^{2+} sensing by calmodulin in complex with a Ca^{2+} channel. *Cell*. 133:1228–1240. https://doi.org/10.1016/j.cell.2008.05.025

Tadross, M.R., and D.T. Yue. 2010. Systematic mapping of the state dependence of voltage- and Ca^{2+}-dependent inactivation using simple open-channel measurements. *J. Gen. Physiol.* 135:217–227. https://doi.org/10.1085/jgp.200910309

Todt, H., S.C. Dudley Jr., J.W. Kyle, R.J. French, and H.A. Fozzard. 1999. Ultra-slow inactivation in mu1 Na^+ channels is produced by a structural rearrangement of the outer vestibule. *Biophys. J.* 76:1335–1345. https://doi.org/10.1016/S0006-3495(99)77296-6

Tuluc, P., B. Benedetti, P. Coste de Bagneaux, M. Grabner, and B.E. Flucher. 2016. Two distinct voltage-sensing domains control voltage sensitivity and kinetics of current activation in CaV1.1 calcium channels. *J. Gen. Physiol.* 147:437–449. https://doi.org/10.1085/jgp.201611568

Van Petegem, F., F.C. Chatelain, and D.L. Minor Jr. 2005. Insights into voltage-gated calcium channel regulation from the structure of the CaV1.2 IQ domain-Ca^{2+}/calmodulin complex. *Nat. Struct. Mol. Biol.* 12:1108–1115. https://doi.org/10.1038/nsmb1027

Van Petegem, F., K.A. Clark, F.C. Chatelain, and D.L. Minor Jr. 2004. Structure of a complex between a voltage-gated calcium channel beta-subunit and an alpha-subunit domain. *Nature*. 429:671–675. https://doi.org/10.1038/nature02588

West, J.W., D.E. Patton, T. Scheuer, Y. Wang, A.L. Goldin, and W.A. Catterall. 1992. A cluster of hydrophobic amino acid residues required for fast Na(+)-channel inactivation. *Proc. Natl. Acad. Sci. USA*. 89:10910–10914. https://doi.org/10.1073/pnas.89.22.10910

Wu, J., Z. Yan, Z. Li, X. Qian, S. Lu, M. Dong, Q. Zhou, and N. Yan. 2016. Structure of the voltage-gated calcium channel Ca(v)1.1 at 3.6 Å resolution. *Nature*. 537:191–196. https://doi.org/10.1038/nature19321

Xia, X.M., B. Fakler, A. Rivard, G. Wayman, T. Johnson-Pais, J.E. Keen, T. Ishii, B. Hirschberg, C.T. Bond, S. Lutsenko, et al. 1998. Mechanism of calcium gating in small-conductance calcium-activated potassium channels. *Nature*. 395:503–507. https://doi.org/10.1038/26758

Yan, Z., Q. Zhou, L. Wang, J. Wu, Y. Zhao, G. Huang, W. Peng, H. Shen, J. Lei, and N. Yan. 2017. Structure of the $Na_v1.4$-β1 complex from electric eel. *Cell*. 170:470–482.e11. https://doi.org/10.1016/j.cell.2017.06.039

Yang, P.S., B.A. Alseikhan, H. Hiel, L. Grant, M.X. Mori, W. Yang, P.A. Fuchs, and D.T. Yue. 2006. Switching of Ca^{2+}-dependent inactivation of Ca(v)1.3 channels by calcium binding proteins of auditory hair cells. *J. Neurosci.* 26:10677–10689. https://doi.org/10.1523/JNEUROSCI.3236-06.2006

Yao, X., S. Gao, and N. Yan. 2022. Structural basis for pore blockade of human voltage-gated calcium channel $Ca_v1.3$ by motion sickness drug cinnarizine. *Cell Res.* 32:946–948. https://doi.org/10.1038/s41422-022-00663-5

Zaydman, M.A., and J. Cui. 2014. PIP2 regulation of KCNQ channels: Biophysical and molecular mechanisms for lipid modulation of voltage-dependent gating. *Front. Physiol.* 5:195. https://doi.org/10.3389/fphys.2014.00195

Zühlke, R.D., G.S. Pitt, K. Deisseroth, R.W. Tsien, and H. Reuter. 1999. Calmodulin supports both inactivation and facilitation of L-type calcium channels. *Nature*. 399:159–162. https://doi.org/10.1038/20200

Supplemental material

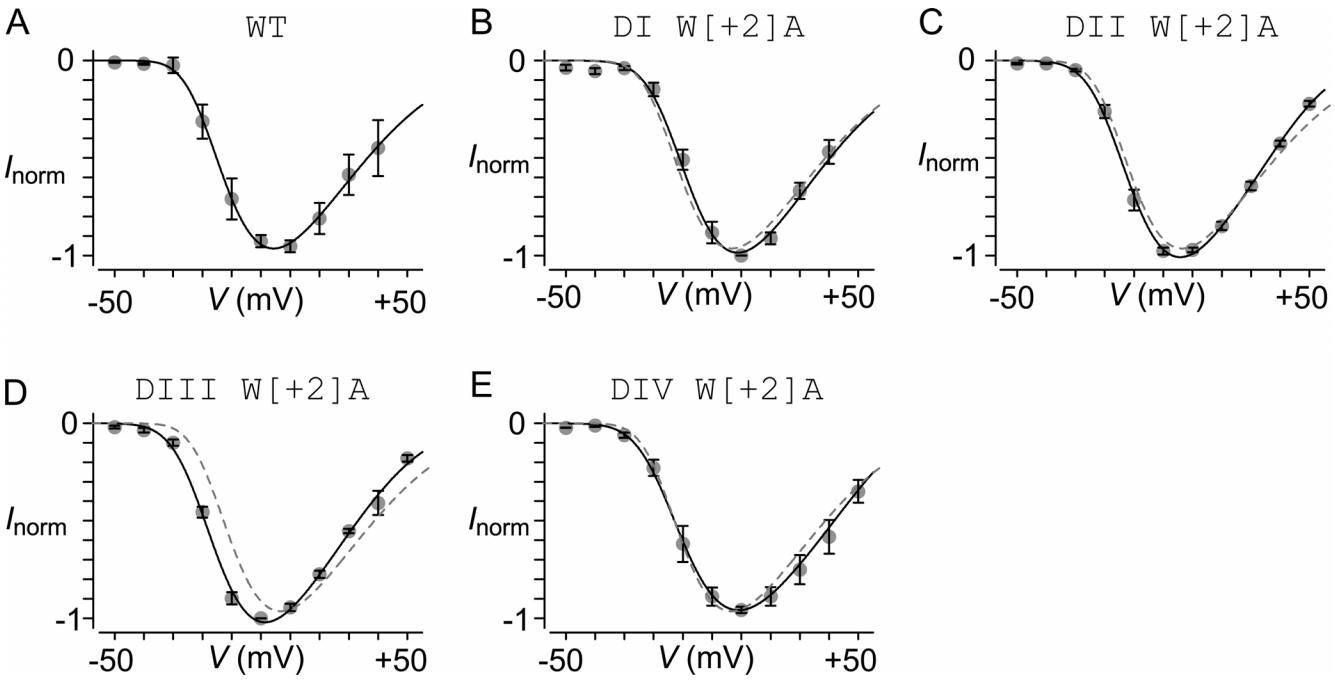

Figure S1. **$Ca_V1.3$ DI–DIV SF mutations minimally perturb channel activation. (A)** Normalized current–voltage relationship for WT $Ca_V1.3$. Each dot, mean ± SEM n = 5 cells. **(B–E)** Normalized IV relations for DI W[+2]A (panel B, n = 5 cells), DII W[+2]A (panel C, n = 6 cells), DIII W[+2]A (panel D, n = 5 cells), and DIV W[+2]A (panel E, n = 7 cells) mutants. In all cases, the change in channel half-activation potential ($V_{1/2}$) was <5 mV.

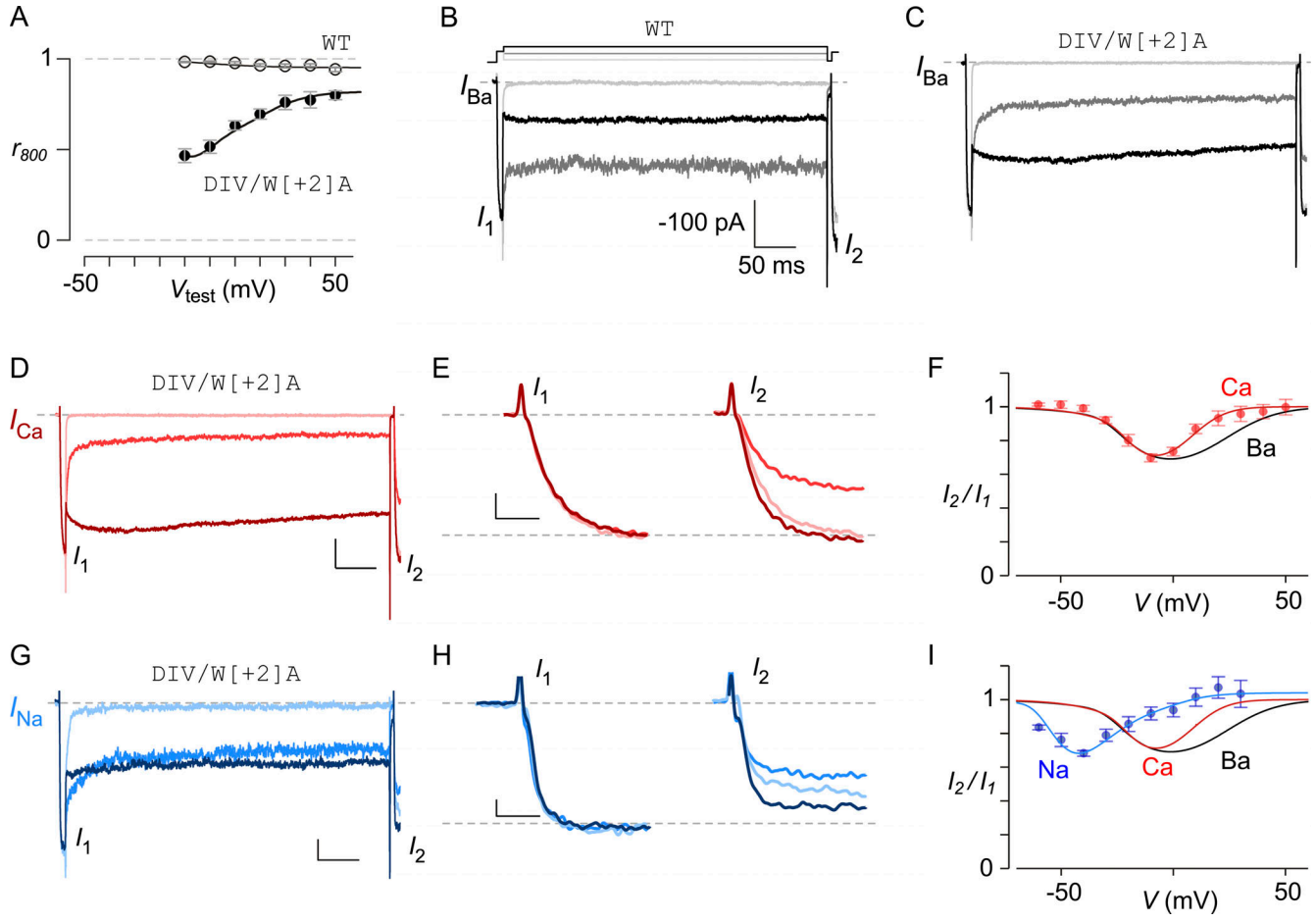

Figure S2. **Extended biophysical characterization of DIV W[+2]A mutation. (A)** Population r_{800} data plotted as a function of test-pulse potential reveals reduced inactivation at higher voltages. Each dot, mean ± SEM. n = 7 cells. **(B)** A two-pulse protocol is used to dissect voltage dependence of inactivation. A brief 15-ms prepulse to 10 mV quantifies available current prior to inactivation. Subsequently, a family of 800-ms voltage steps (test pulse) is used to evoke steady-state inactivation and a 15-ms postpulse is then used to quantify the current remaining following VDI. The extent of inactivation is quantified as the ratio of peak currents during postpulse to prepulse. Exemplar currents at three different test pulse potentials (light gray, −50 mV; gray, 0 mV; and black +50 mV) are shown. Exemplar trace for wild-type $Ca_V1.3$. Further analysis in Fig. 2, C and E. **(C)** Exemplar trace for DIV W[+2]A mutation. Further analysis in Fig. 2, D and F. **(D–F)** VDI of DIV W[+2]A probed in the presence of Ca^{2+} as charge carrier. Panel D, exemplar trace. Panel E, comparison of Ca^{2+} currents during prepulse (left, I_1) versus postpulse (right, I_2). Note that the current magnitude during the postpulse is maximally reduced at intermediate voltages. Panel F, population data shows U-shaped dependence of inactivation with Ca^{2+} as the charge carrier (red). Black trace, relationship with Ba^{2+} as the charge carrier reproduced from Fig. 2 F. Each dot, mean ± SEM, n = 8 cells. **(G–I)** VDI of DIV W[+2]A mutation with Na^+ (but no divalents) as charge carrier. Format as in panels D–F. n = 7 cells.